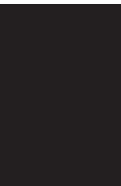




Surface Nanoscience

Guest Editors: Rakesh K. Joshi, Masamichi Yoshimura,
and Kazuyuki Ueda





Surface Nanoscience

Journal of Nanomaterials

Surface Nanoscience

Guest Editors: Rakesh K. Joshi,
Masamichi Yoshimura, and Kazuyuki Ueda



Copyright © 2007 Hindawi Publishing Corporation. All rights reserved.

This is a special issue published in volume 2007 of “Journal of Nanomaterials.” All articles are open access articles distributed under the Creative Commons Attribution License, which permits unrestricted use, distribution, and reproduction in any medium, provided the original work is properly cited.

Editor-in-Chief

Michael Z. Hu, Oak Ridge National Laboratory, USA

Advisory Board

James Adair, USA
Jeff Brinker, USA
Taeghwan Hyeon, South Korea

Nathan Lewis, USA
Alon McCormick, USA
Gary Messing, USA

Z. L. Wang, USA
Alan Weimer, USA
Jackie Ying, USA

Associate Editors

John Bartlett, Australia
Michael Harris, USA
Do Kyung Kim, South Korea

S. J. Liao, China
Jun Liu, USA
S. Mathur, Germany

Michael S. Wong, USA
M. Yoshimura, Japan

Editorial Board

Donald A. Bansleben, USA
Siu Wai Chan, USA
Gang Chen, USA
Sang-Hee Cho, South Korea
Chunxiang Cui, China
Ali Eftekhari, Iran
Claude Estournes, France
Alan Fuchs, USA
Lian Gao, China
Hongchen Gu, China
Justin Holmes, Ireland

David Hui, USA
Rakesh K. Joshi, Japan
Alan Lau, Hong Kong
Butrand I. Lee, USA
J. Li, Singapore
J. -Y. Liu, USA
Songwei Lu, USA
Ed Ma, USA
Pierre Panine, France
Donglu Shi, USA
Bohua Sun, South Africa

Y. Wang, USA
Xiaogong Wang, China
E. G. Wang, China
C. P. Wong, USA
Ping Xiao, UK
Zhili Xiao, USA
Nanping Xu, China
Doron Yadlovker, Israel
Peidong Yang, USA
Zhenzhong Yang, China
Kui Yu, Canada

Contents

Surface Nanoscience, Rakesh K. Joshi, Masamichi Yoshimura, and Kazuyuki Ueda
Volume 2007, Article ID 71869, 1 page

Shape of Field-Induced Nanostructures Formed by STM, Subhashis Gangopadhyay, Asit Kumar Kar, and Balbir Kumar Mathur
Volume 2007, Article ID 36435, 5 pages

Effect of Current Density on Thermodynamic Properties of Nanocrystalline Palladium Capped Samarium Hydride Thin Film Switchable Mirrors, Pushpendra Kumar and L. K. Malhotra
Volume 2007, Article ID 52083, 7 pages

Size-Selected SnO_{1.8} : Ag Mixed Nanoparticle Films for Ethanol, CO, and CH₄ Detection, Rakesh Kumar Joshi and Frank Einar Kruis
Volume 2007, Article ID 67072, 5 pages

Effect of Silver Addition on the Ethanol-Sensing Properties of Indium Oxide Nanoparticle Layers: Optical Absorption Study, Vidya Nand Singh, Bodh Raj Mehta, Rakesh Kumar Joshi, and Frank Einar Kruis
Volume 2007, Article ID 28031, 5 pages

Catalyst Composition and Content Effects on the Synthesis of Single-Walled Carbon Nanotubes by Arc Discharge, Tingkai Zhao, Qinghu Tang, Yongning Liu, Changchun Zhu, and Xiang Zhao
Volume 2007, Article ID 84540, 4 pages

Effect of Etching Parameter on Pore Size and Porosity of Electrochemically Formed Nanoporous Silicon, Pushpendra Kumar and Patrick Huber
Volume 2007, Article ID 89718, 4 pages

Editorial

Surface Nanoscience

Rakesh K. Joshi, Masamichi Yoshimura, and Kazuyuki Ueda

Nano High Tech Research Center, Toyota Technological Institute, Nagoya 468-8511, Japan

Received 16 May 2007; Accepted 16 May 2007

Copyright © 2007 Rakesh K. Joshi et al. This is an open access article distributed under the Creative Commons Attribution License, which permits unrestricted use, distribution, and reproduction in any medium, provided the original work is properly cited.

Surface science has been always a matter of nanoscience even before the beginning of nanotechnology in modern science. Dealing with physics and chemistry of surfaces in materials science is the platform for engineers and scientists to play in nanometer scale. Surface science changes the scale of scientific research from micrometers to nanometers and makes the nanotechnology more complete. The surface analyses of semiconductors and metals are of interest for basic research and technological applications. The surface dependent phenomenon, which occur due to the modifications in the surface states of materials extend the applicability of the materials. The surface science became very much interesting in the present nanotechnology era. In present scenario, the application of materials is dominantly determined by its surface behavior because of the high surface-to-volume ratio in the nanomaterials. Clearly, surface nanoscience has immense potential to declare the utility of materials for various applications.

This special issue of the Journal of Nanomaterials is dedicated to basic and applied surface science for nanomaterials. It has 6 articles from different fields of materials science in nanoscale. Scanning probe microscopy, which is the most important topic for surface scientists, is discussed in an article written by Gangopadhyay et al. The authors have studied the shape of field-induced nanostructures formed by scanning tunneling microscopy and discussed the formation mechanism of nanostructures.

Surface chemistry, with electrochemical techniques, has also been covered in the present issue. In the article written by Kumar and Malhotra, they have studied the switchable mirrors and presented the effect of current density on thermodynamic properties of nanocrystalline palladium capped samarium hydride thin film switchable mirrors. They conclude that the nanocrystalline Pd capped Sm films can be reversibly switched between the metallic reflecting dihydride

state to semiconducting transparent nearly trihydride state by loading/deloading of hydrogen.

Gas sensing behavior, with surface area dependence, is discussed in two papers. The article written by Joshi and Kruis shows the distinction between size effect and specific surface area effect in the ethanol gas sensing behavior of $\text{SnO}_{1.8}$:Ag nanoparticle films and gives evidence of the dominance of size effect of the metal dopant over the surface area effect in the gas sensing of the films. The authors have also demonstrated the use of $\text{SnO}_{1.8}$:Ag for CH_4 and CO detection. In the article written by Singh et al., the authors have made correlation between optical absorption analysis and gas sensing properties of In_2O_3 :Ag nanoparticle layers.

One very interesting article by Zhao et al., discusses the synthesis and application of carbon nanotubes, which is a topic of prime interest at present. The authors report the synthesis of single-walled carbon nanotubes by modified arc discharging furnace using Fe-Ni-Mg powders as catalyst.

Effect of etching parameter on pore size and porosity of electrochemically formed nanoporous silicon is presented in an article by Kumar and Huber. This article is very useful for the scientists working in the field of porous silicon.

*Rakesh K. Joshi
Masamichi Yoshimura
Kazuyuki Ueda*

Research Article

Shape of Field-Induced Nanostructures Formed by STM

Subhashis Gangopadhyay, Asit Kumar Kar, and Balbir Kumar Mathur

Department of Physics and Meteorology, Indian Institute of Technology, Kharagpur 721302, India

Received 13 September 2006; Accepted 11 October 2006

Recommended by Rakesh K. Joshi

Creation of controlled and reproducible nanostructures on material surfaces using scanning tunneling microscope is a novel technique, which can be used for a variety of applications. We have examined the shape of the nanostructures so formed on the gold film using tungsten tip and examined the formation parameters, which govern their shape and size. During our investigations it is found that the reproducibility of mound formation can reach up to 90% under optimum operating conditions, whereas the pit formation can be made with almost 100% reproducibility. Formation mechanism of such nanostructures is also discussed.

Copyright © 2007 Subhashis Gangopadhyay et al. This is an open access article distributed under the Creative Commons Attribution License, which permits unrestricted use, distribution, and reproduction in any medium, provided the original work is properly cited.

1. INTRODUCTION

Formation of field-induced nanostructures on thin films and on plane surfaces has been carried out by a large number of groups [1–5]. Controlled and reproducible modification of surfaces on a nanometer scale or even on an atomic scale has been projected to be of great technological as well as fundamental importance. Theoretical investigations on the mechanism of nanostructure formation are quite informative and provide substantial insight.

Different techniques to modify the surface using STM can broadly be classified into three categories. In the first category, atoms are transferred at specific sites using electrostatic adherence of atoms to the tip [6, 7]. Second technique is to create mounds and pits on the substrate by locally destroying the surface, that is, mechanically scratching the surface with the tip [8]. And the third is to produce the same structure by applying a voltage pulse between the tip and the sample surface [9–23]. In the process of mechanical scratching, the tip loses its sharpness, thereby making it ineffective for subsequent topographic application. But in the tip-bias pulsing method, it is well controlled and nondestructive. In this pulse-writing method, the main control parameters are the sign, magnitude, duration, and the number of voltage pulse applied between the tip and sample surface.

The most used technique is the bias-pulse technique. Nanostructures formed by this technique can again be classified into two broad categories: the pit (valley) [19, 23] and the mound (hill) [7, 10, 12–15, 17, 18]. In case of forming

a pit, the sample material is scooped out from the surface. There are various processes to take out the sample from the surface such as mechanical contact [10, 13] or evaporation of the material by field effect or local melting [9, 11, 12]. In the case of mound formation, the sample is added to the surface [15] or some plastic deformation [14] may take place.

Formation of a pit or a mound is reproducible to a very large extent as has been reported in a large number of publications and during our own investigations. But what concerns us at this stage is that at times we attempt to form a pit but gets a mound instead or sometimes the other way around. With known parameters controlling the metamorphism (like pulse height, polarity, duration, repetition, etc.), we have attempted to create many nanostructures on gold films by bias-pulse technique using a tungsten tip. We describe the most possible formation of pit and mound and its dependence on parameters like the pulse height, polarity, set current for the pulse, and the nature of the tip structure. STM is operated in air ambient at room temperature and the gold film is chosen because of its lower threshold for field evaporation and oxide protective inert nature. We also discuss the possible physical mechanism regarding the phenomenon.

2. EXPERIMENT

Thin films of gold (500 Å) have been deposited on the various substrates (silicon, mica, and glass), by thermal evaporation method in the physical vapor deposition (PVD) unit, at a base pressure of 10^{-6} T at room temperature. The

films are subsequently transferred into the STM (model UHV- 635, RHK Technology, Inc.) chamber. An electrochemically etched [24] tungsten wire of diameter 0.35 μm is used as a STM tip for the topographic tunneling and nanomodification of the gold surface. Applying bias pulse between the tip and the surface nanoscale structures has been created. For the topographic data recording, the STM is operated in the constant current mode using a feed back loop. Throughout the scanning, the bias voltage is maintained at a fixed value. The tip is scanned over the surface and the topographic data is stored as 256×256 data point in the SM2 file format.

The movement of the tip and the sample are well controlled by a piezo tube. The sample, fixed on sample holder, is placed on a piezo tube and the position of the sample below the tip can be adjusted by controlling the voltage applied to the offset piezo. This facility permits us to shift the sample in a precisely controlled manner so as to position the tip at a required location at the surfaces.

In our STM, the tip is grounded and the bias voltage is supplied to the sample surface. The STM is operated at various bias voltages (~ 100 mV) and also the tunneling current (~ 100 pA) is varied to get the good topographic image. Prior to the surface modification, smooth areas are selected by scanning the large areas at different locations on the sample surface. To form the nanostructure the bias pulse is applied in the range of 2–10 V and the duration of each pulse is kept fixed at 1 ms. To study the dependence of the shape of the nanostructure on tip-sample separation, the set current is varied for various pulses. The probability of formation of mound and pit is dependent on the height of the applied pulse. A statistical analysis of the probability of formation of mound and pit is done applying the pulses of various heights. The spectroscopic studies of the surface materials are done before and after formation of mound by applying a bias pulse.

3. RESULTS AND DISCUSSION

Nanostructures created by bias-pulse technique ranges from simple mound and pit to complex formation. For certain settings, the probability of reproducibility goes as high as 90% whereas for others it may be lower. Figure 1 illustrates the point that using the same tip, under similar operating conditions different surface modifications can be formed. Figures 1(a) and 1(b) are clear cases of mound formation but Figure 1(c) depicts a damage grain boundaries. At another location four pulses were applied and grain coalescence appears to have taken place (Figure 1(d)). In only 10% cases unclear pit formation was detected (Figure 1(e)). As the pulse height is increased to 4 V, the probability of clear mound formation increases to 90%. At 5 V, the probability of mound formation decreases and pits become clearer (Figure 2). Figure 2(a) is a clear case of mound formation whereas Figures 2(b) and 2(c) are complex formations. The pit seen in Figure 2(d) is also formed while operating the system under similar conditions as in Figures 2(a), 2(b), and 2(c). As the bias pulse increases, the probability of pit formation increases. Figure 3 shows the probability of a different

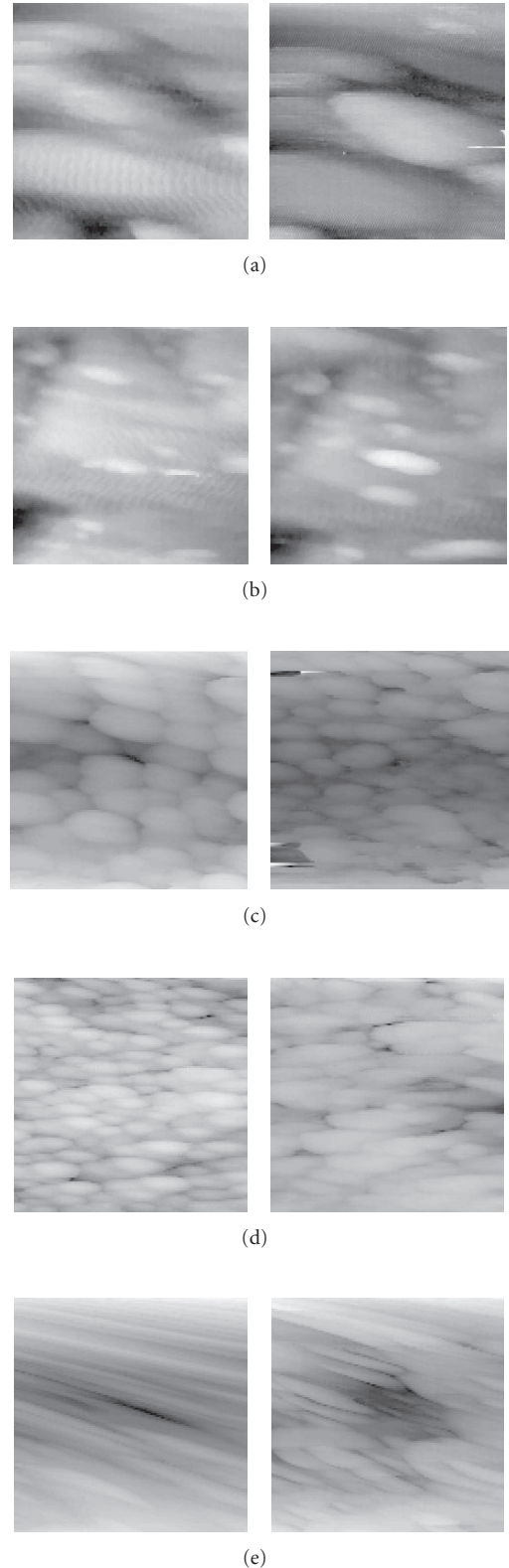


FIGURE 1: Surface topographs of the gold films on silicon, before (left side) and after (right side) applying the bias pulse of 3 V with tip-surface separation corresponding to tunneling current of 300 pA. Scan areas are (a) $100 \times 100 \text{ nm}^2$; (b) $200 \times 200 \text{ nm}^2$; (c) $250 \times 250 \text{ nm}^2$; (d) $300 \times 300 \text{ nm}^2$; and (e) $500 \times 500 \text{ nm}^2$, respectively.

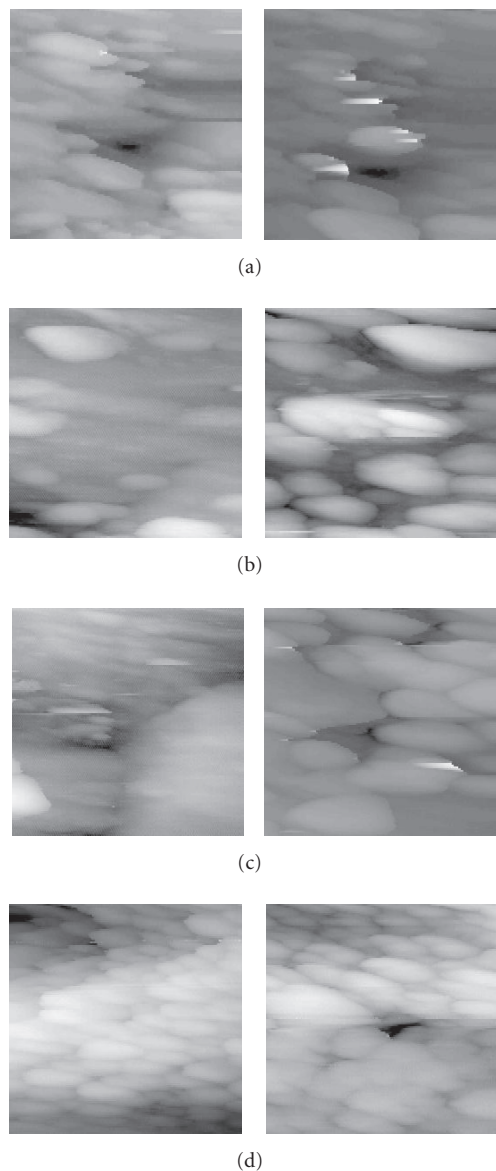


FIGURE 2: Surface topographs of the gold films on silicon, before (left side) and after (right side) applying the bias pulse of 5 V with tip-surface separation corresponding to tunneling current of 300 pA. Scan areas are (a) $200 \times 200 \text{ nm}^2$; (b) $200 \times 200 \text{ nm}^2$; (c) $200 \times 200 \text{ nm}^2$; and (d) $300 \times 300 \text{ nm}^2$, respectively.

distinct nanostructure formation, which could occur due to bias pulse.

This raises the question whether any other considerations determine the reproducibility. In this simple case study, gold films had been deposited on pieces of silicon wafer cut out from the same 4-inch wafer obtained from m/s Wafer World Inc., USA, under identical operating conditions. Surface topographs taken before the application of bias pulse were also identical. One way to generalize it is to consider different types of surface modifications under the same mechanism. It may be local melting, local plastic deformation due to sudden change of electrostatic field, or may be local transfer of

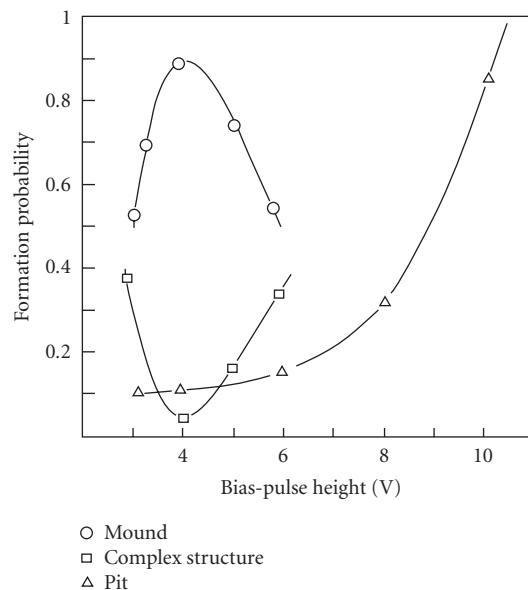


FIGURE 3: Dependence of the formation probability of different type of nanostructures on bias pulse.

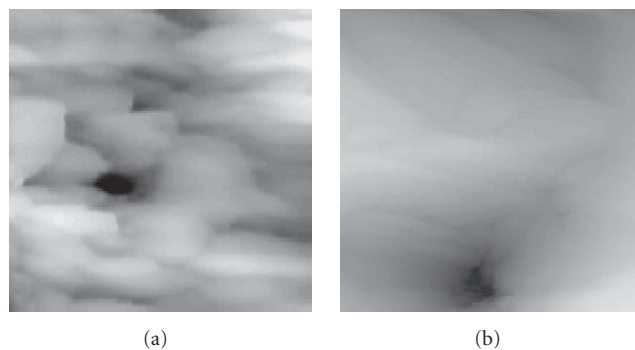


FIGURE 4: Change in the pit shape due to change in tip-surface distance. Both are taken using 3 V pulse but in (a) the tip-surface separation corresponds to tunneling current of 300 pA (scan area $280 \times 280 \text{ nm}^2$) while in (b) the tip-surface separation corresponds to 2 nA tunneling current (scan area $500 \times 500 \text{ nm}^2$).

material. Hence, the shape of the nanostructures so formed must depend on local defect structure of the film.

Another important consideration is the tip-surface separation. If this separation is decreased (by increasing set-tunneling current) the formations are well defined. All modifications shown in Figures 1 and 2 were carried out at setting the tip-sample separation corresponding to tunneling current of 0.3 nA. Now we compare pits formed at set currents of 0.3 nA and those formed at 2.0 nA as shown in Figure 4. The crater in Figure 4(b) is deeper (33 nm) and wider (100 nm) as compared to the one in Figure 4(a).

In order to investigate the effect of substrate, we have carried out similar experiment of films deposited on mica and

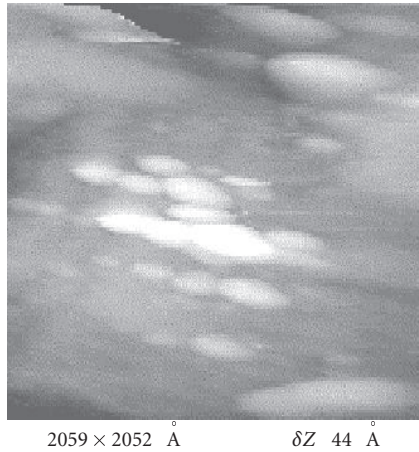
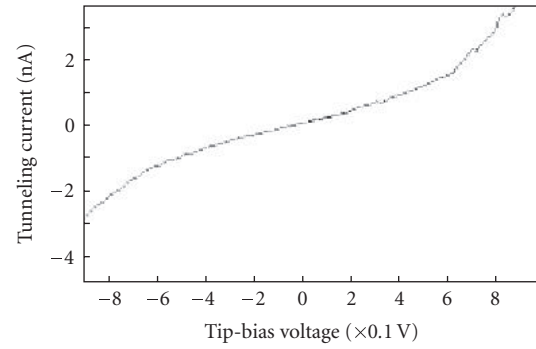


FIGURE 5: Multiple mound formation (scan area $200 \times 200 \text{ nm}^2$).

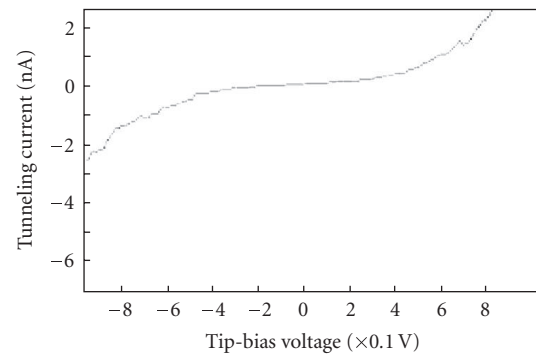
glass substrates. Results are similar and do not justify inclusion of additional topographs.

We illustrate two main factors, which determine the formation of good nanostructures. Looking at Figure 5, it is seen that a multimound formation is repeated at many locations of the topograph. These are produced due to application of single bias pulse. The possible causes of this defect are (a) the tip is likely to have three sharp-pointed corners and (b) some sort of switch debounce must have taken place in the electronics and an associated shake in either the tip-position or the surface or both. The multipoint tip does not effect the topography because the tunneling takes place predominantly from the point closest to the surface. But at the time of high field pulse applied between the tip and the sample, all the pointed corners generate different fields on the surface, thereby, creating multiple hillock of different size [14].

Our investigations support the theory proposed by Tsong regarding mechanism of nanostructure formation [9, 11, 12]. Such metamorphism is attributed to a local melting of the sample surface. It is seen that for the lower value of voltage pulse the probability of formation of mound is dominating. That can be explained as due to the voltage pulse, a high electric field is generated causing the local melting of the gold surface. Due to the high electrostatic force, the molten material is attracted towards the tip and creates a plastic deformation instead of pure elastic deformation [14]. In case of higher voltage pulse it is seen that the probability of pit formation is dominating. In this case the electrostatic field is sufficiently high to cause local field evaporation instead of melting. Formation of mound is not likely to be due to the material transfer from tip to surface, which can be explained as follows. We observed that even after repeated use of tip in the field application mode, the tip quality does not deteriorate and is capable of producing good quality reproducible topographs [14, 16–18]. Secondly, the possibility of transfer of atoms by field evaporation between tip and sample atoms is depending on the binding energy. As the binding energy of tungsten atom is greater than that of gold [9], the transfer of tip material (tungsten) to the surface (gold) is least likely. An-



(a)



(b)

FIGURE 6: Tunneling spectra before and after formation of a mound.

other support, which negates material transfer, is the similarity between tunneling I-V spectra obtained before and after the formation of nanostructure and with tip positioned on the mound (Figure 6). Slight change in the STS spectra is likely to be caused by the change in electronic state of the surface atoms due to high voltage pulse.

4. CONCLUSION

Using scanning tunneling microscope, different types of nanostructures have been formed. The possibility of the formation of various structures (mound, pit, and complex structures) with different pulse height has been studied. It is seen that for gold film on silicon, the probability of mound formation is higher for bias-pulse height below 6 V. At higher voltage, a pit is more likely to form. The effect of set current on nanostructure formation is also investigated. The possible mechanism behind the nanostructure formation is attributed to local melting (mound formation) for lower bias-pulse voltage and to local vaporization (pit formation) for higher bias-pulse voltage.

ACKNOWLEDGMENT

We are grateful to the Department of Science and Technology, Council of Scientific and Industrial Research, Government of India, for financial assistance in this project.

REFERENCES

- [1] S. P. Wilks, T. G. G. Maffei, G. T. Owen, K. S. Teng, M. W. Penny, and H. Ferkel, "Charge writing on the nanoscale: from nanopatterning to molecular docking," *Journal of Vacuum Science & Technology B: Microelectronics and Nanometer Structures*, vol. 22, no. 4, pp. 1995–1999, 2004.
- [2] T. G. G. Maffei, G. T. Owen, M. W. Penny, H. S. Ferkel, and S. P. Wilks, "STM patterning of SnO₂ nanocrystalline surfaces," *Applied Surface Science*, vol. 234, no. 1–4, pp. 2–10, 2004.
- [3] K. Sattler, "Nanolithography using the scanning tunneling microscope," *Japanese Journal of Applied Physics*, vol. 42, no. 7 B, pp. 4825–4829, 2003.
- [4] Th. Schimmel, H. Fuchs, S. Akari, and K. Dransfeld, "Nanometer-size surface modifications with preserved atomic order generated by voltage pulsing," *Applied Physics Letters*, vol. 58, no. 10, pp. 1039–1041, 1991.
- [5] E. S. Snow, P. M. Campbell, and P. J. McMarr, "Fabrication of silicon nanostructures with a scanning tunneling microscope," *Applied Physics Letters*, vol. 63, no. 6, pp. 749–751, 1993.
- [6] D. M. Eigler, C. P. Lutz, and W. E. Rudge, "An atomic switch realized with the scanning tunnelling microscope," *Nature*, vol. 352, no. 6336, pp. 600–603, 1991.
- [7] D. M. Eigler and E. K. Schweizer, "Positioning single atoms with a scanning tunnelling microscope," *Nature*, vol. 344, no. 6266, pp. 524–526, 1990.
- [8] U. Landman and W. D. Luedtke, "Consequences of tip-substrate interactions," in *Scanning Microscopy III*, R. Wiesendanger and H. J. Guntherodt, Eds., chapter 9, p. 207, Springer, Berlin, Germany, 1993.
- [9] T. T. Tsong, "Effects of an electric field in atomic manipulations," *Physical Review B*, vol. 44, no. 24, pp. 13703–13710, 1991.
- [10] J. I. Pascual, J. Méndez, J. Gómez-Herrero, A. M. Baró, N. García, and V. T. Binh, "Quantum contact in gold nanostructures by scanning tunneling microscopy," *Physical Review Letters*, vol. 71, no. 12, pp. 1852–1855, 1993.
- [11] U. Gratzke and G. Simon, "Mechanism of nanostructure formation with the scanning tunneling microscope," *Physical Review B*, vol. 52, no. 11, pp. 8535–8540, 1995.
- [12] U. Gratzke and G. Simon, "New mechanism of nanostructure formation with the STM," *Microelectronic Engineering*, vol. 27, no. 1–4, pp. 35–38, 1995.
- [13] R. Taylor, R. S. Williams, V. L. Chi, et al., "Nanowelding: tip response during STM modification of Au surfaces," *Surface Science*, vol. 306, no. 1–2, pp. L534–L538, 1994.
- [14] V. Srinivas, M. V. H. Rao, B. K. Mathur, and K. L. Chopra, "Creation of nanostructures on nickel thin films by STM," *Bulletin of Materials Science*, vol. 17, no. 6, pp. 841–848, 1994.
- [15] R. S. Becker, J. A. Golovchenko, and B. S. Swartzentruber, "Atomic-scale surface modifications using a tunnelling microscope," *Nature*, vol. 325, no. 6103, pp. 419–421, 1987.
- [16] H. J. Mamin, S. Chiang, H. Brik, P. H. Guethner, and D. Rugar, "Gold deposition from a scanning tunneling microscope tip," *Journal of Vacuum Science & Technology B: Microelectronics and Nanometer Structures*, vol. 9, no. 2, pp. 1398–1402, 1991.
- [17] H. J. Mamin, P. H. Guethner, and D. Rugar, "Atomic emission from a gold scanning-tunneling-microscope tip," *Physical Review Letters*, vol. 65, no. 19, pp. 2418–2421, 1990.
- [18] S. E. McBride and G. C. Wetsel Jr., "Nanometer-scale features produced by electric-field emission," *Applied Physics Letters*, vol. 59, no. 23, pp. 3056–3058, 1991.
- [19] Y. Z. Li, L. Vazquez, R. Piner, R. P. Andres, and R. Reifenger, "Writing nanometer-scale symbols in gold using the scanning tunneling microscope," *Applied Physics Letters*, vol. 54, no. 15, pp. 1424–1426, 1989.
- [20] U. Staufer, R. Wiesendanger, L. Eng, et al., "Surface modification in the nanometer range by the scanning tunneling microscope," *Journal of Vacuum Science & Technology A: Vacuum, Surfaces, and Films*, vol. 6, no. 2, pp. 537–539, 1988.
- [21] U. Staufer, R. Wiesendanger, L. Eng, et al., "Nanometer scale structure fabrication with the scanning tunneling microscope," *Applied Physics Letters*, vol. 51, no. 4, pp. 244–246, 1987.
- [22] J. Schneir, R. Sonnenfeld, O. Marti, P. K. Hansma, J. E. Demuth, and R. J. Hamers, "Tunneling microscopy, lithography, and surface diffusion on an easily prepared, atomically flat gold surface," *Journal of Applied Physics*, vol. 63, no. 3, pp. 717–721, 1988.
- [23] I.-W. Lyo and Ph. Avouris, "Field-induced nanometer- to atomic-scale manipulation of silicon surfaces with the STM," *Science*, vol. 253, no. 5016, pp. 173–176, 1991.
- [24] A. K. Kar, S. Gangopadhyay, and B. K. Mathur, "Reverse electrochemical floating-layer technique of SPM tip preparation," *Measurement Science and Technology*, vol. 11, no. 10, pp. 1426–1431, 2000.

Research Article

Effect of Current Density on Thermodynamic Properties of Nanocrystalline Palladium Capped Samarium Hydride Thin Film Switchable Mirrors

Pushpendra Kumar^{1,2} and L. K. Malhotra²

¹ *Technische Physik, Universität des Saarlandes, Geb. 38, Postfach 151150, 66041 Saarbrücken, Germany*

² *Thin Film Laboratory, Department of Physics, Indian Institute of Technology, Hauz Khas, New Delhi 110016, India*

Received 20 November 2006; Accepted 12 December 2006

Recommended by Rakesh K. Joshi

A 55 nm samarium film capped with a 10 nm palladium overlayer switched from a metallic reflecting to a semiconducting, transparent in visible state during ex-situ hydrogen loading via electrochemical means in 1 M KOH electrolytic aqueous solution at room temperature. The switching between metal to semiconductor was accompanied by measurement of transmittance during hydrogen loading/unloading. The effect of current density on switching and thermodynamic properties was studied between dihydride state (FCC phase) and trihydride state (hexagonal phase). From the plateau of partial pressure of hydrogen at $x = 2.6$, enthalpy of formation was calculated at different current densities. The diffusion coefficients and switching kinetics are shown to depend on applied current density.

Copyright © 2007 P. Kumar and L. K. Malhotra. This is an open access article distributed under the Creative Commons Attribution License, which permits unrestricted use, distribution, and reproduction in any medium, provided the original work is properly cited.

1. INTRODUCTION

Hydrogen in metal has been the subject of extensive research because of their intriguing physical and chemical properties [1]. Recently, Huijberts et al. [2] have discovered electrical and optical switching in yttrium and lanthanum thin film just by varying the hydrogen concentration. This switchable mirror effect has since received a lot of attention both from fundamental physics [3–5] point of view as well as its technological applications in smart windows, hydrogen sensors, solid-state displays, and electrochromic devices [6]. It is now known that almost all rare earth metals and rare earth-based alloys exhibit this effect [7–14]. Hydrogenation of palladium-capped thin films of these materials can be achieved by exposing the sample to a hydrogen gas atmosphere [15–20], electrochemically by polarization in a suitable electrolyte solution [21–23] or chemically by immersion in a NaBH₄ solution [24]. Because of the hazards involved in handling hydrogen gas [25], and the difficulty in continuously monitoring the amount of hydrogen getting incorporated into the films, gas phase loading is not very practical from the application point of view. These issues can be taken care of by hydrogenation via electrochemical means. Electrochemical

loading offers many advantages: the concentration of hydrogen in the film can be controlled accurately, extremely low pressure can be achieved and electrochemical potential is related to an effective hydrogen gas pressure, thereby offering the possibility to study the thermodynamic properties of the system. Drastic changes in optical properties have been observed in cases where there is a structural transition in going from the dihydride to trihydride state as well as in cases where the structure remains unaffected confirming thereby that the phenomenon is of electronic origin [3]. In this study, we report the thermodynamic properties of Pd/Sm thin film between dihydride state to trihydride state in open circuit and different anodically polarizing condition. The results are presented in this paper.

2. EXPERIMENTAL

Sm films of thickness 55 nm were deposited by vacuum evaporation on 40 mm × 40 mm × 2 mm ultrasonically cleaned glass substrates. The base pressure in the vacuum system was 7×10^{-5} Pa prior to deposition. Pd overlayer of thickness 10 nm was deposited on top of the Sm films without breaking the vacuum. The experimental details for insitu

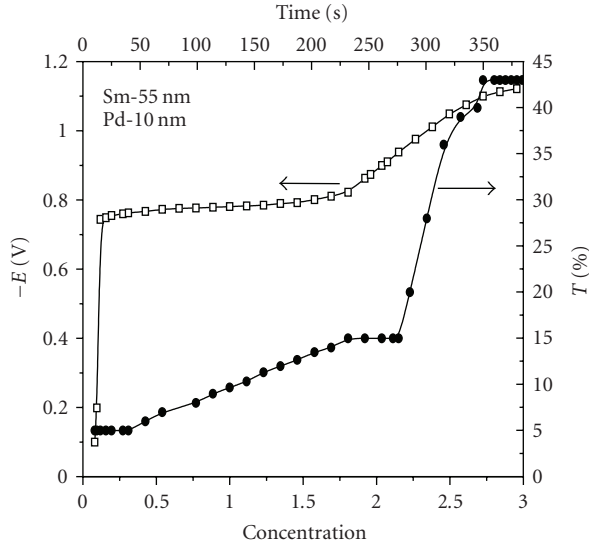


FIGURE 1: Change of the electrode potential and transmission of Pd (10 nm) capped Sm film (55 nm) on hydrogen loading at 0.2 mA/cm^2 as a function of hydrogen concentration $x = \text{H/Sm}$ determined from galvanostatic loading experiments.

measurement of film thickness and rate of deposition have been described in one of the earlier papers [26]. The galvanostatic intermittent titration technique (GITT) was used to determine the equilibrium potential as a function of hydrogen concentration in the sample. The electrochemical measurements were performed in an aqueous 1 M KOH solution using a Pt strip as a counter electrode and an Hg/HgO electrode as a reference electrode. The effective area of palladium capped samarium films exposed to 1 M KOH electrolyte solution was 4.9 cm^2 [27]. All potentials were measured with respect to the reference electrode using an electrometer (Keithley, Model-6517A) and constant current source (Keithley, Model-224) was used to apply the current. For in situ optical transmission, the Pd capped Sm film (WE) was illuminated with a diode laser (LA 12-10 –650 nm) and the transmission intensity measured with a photodyne radiometer/photometer (Model 88XLA), placed on the opposite end. Before each measurement, high-purity argon gas was bubbled through the solution at least for 15 minutes to remove the oxygen and a constant argon flow was maintained over the electrolyte during the measurements. Atomic force microscopy (Veeco nanoscope IIIa) was used to study the surface morphology.

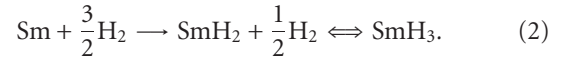
3. RESULTS AND DISCUSSION

During electrochemical loading, the electrolytic reduction of a proton donating species, water in our case, results in the following reaction:



The mechanism of hydrogen entry into palladium involves proton discharge $\text{H}^+ + \text{e}^- \rightarrow \text{H}$ followed by immediate hydrogen adsorption in the palladium layer. The adsorbed hydrogen subsequently diffuses into the underlying Sm film and is absorbed therein.

The reaction of hydrogen with Sm proceeds as follows:



The second step is a reversible transition, which can easily be induced by changing the polarity of the cell or in open circuit condition, whereas the first step is unidirectional. This is because of the relative small heat of formation for the second step (-39.6 kJ/mol H) compared to the heat of formation for the first step (-202.6 kJ/mol H) [11].

The measured electrode potential (E) between WE and reference electrode, transmittance (T) of the WE, as a function of hydrogen concentration getting incorporated in the WE on applying a constant current density $i = 0.2 \text{ mA/cm}^2$, are plotted in Figure 1. Figure 1 shows that the potential of WE drops from -0.190 V to -0.76 V immediately after applying the constant current. This immediate drop in potential is due to excess charge accumulated on the interface of electrolyte and WE. Three regions can thereafter be clearly distinguished: (i) a near plateau from -0.76 V to -0.81 V , (ii) a gradual drop in potential from -0.81 V to -1.11 V , and again (iii) a constancy at $\sim -1.11 \text{ V}$. Transmittance curves taken during hydrogen loading is also shown in Figure 1. Five regions can be distinguished in the transmittance curve. T is initially almost constant at 5% and then rises gradually to attain a value of 15%. It again remains constant for some time followed by a sharper rise in its value to 43% and then remaining constant at that value thereafter. Since hydrogen is getting incorporated in the Sm film due to the passage of current, these changes in the two curves represent the changes taking place in Sm film due to the incorporation of hydrogen. The detailed explanation of these changes on hydrogen uptake has been discussed in one of our earlier paper [27]. Using Faraday's law and taking the film thickness, the electrode surface area, and the integrated charge into account, we have calculated the hydrogen concentration in Sm film. Based on an earlier report [28], we have taken an initial hydrogen concentration $x = 0.08$, which gets incorporated into the film during deposition, into account while making our calculations. It is very important that the thickness taken into account while calculating hydrogen concentration is measured very accurately.

The working electrode was then reversibly switched, in a 1 M KOH electrolytic aqueous solution, between dihydride state (dark brownish color) and trihydride state (golden greenish color) galvanostatically at different constant current densities (0.2, 0.6, 1.02, 2.04 mA/cm^2). A different current density was applied for different time periods to attain an appropriate amount of hydrogen in the film. Figure 2(a) shows the change in potential with time on loading of hydrogen.

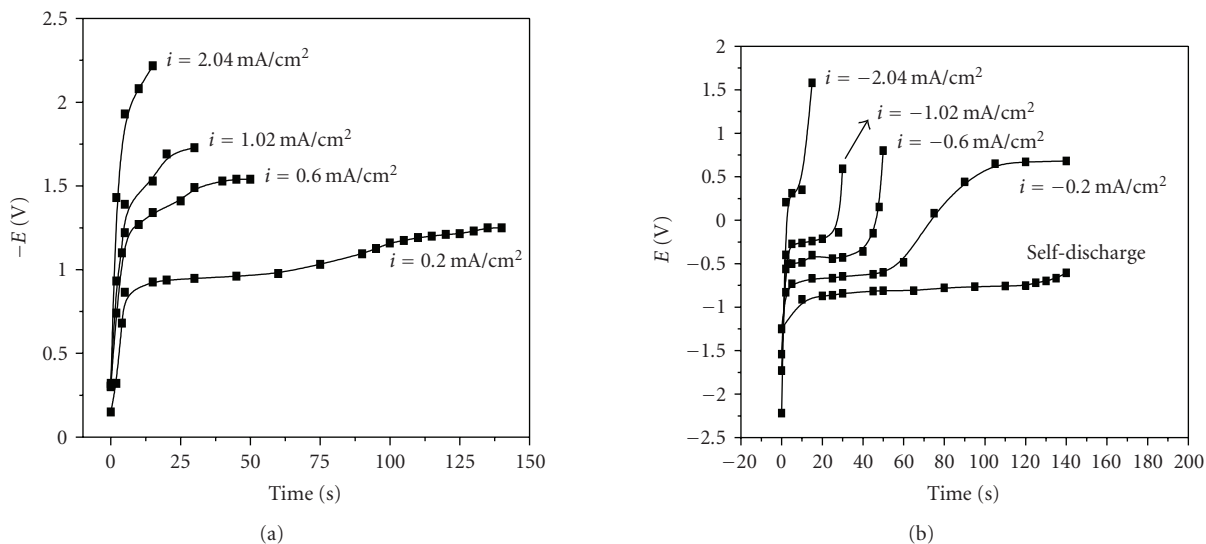


FIGURE 2: Change of the electrode potential with time for several current densities: (a) loading (b) unloading.

The fall in potential directly depends on applied current density between working and counter electrodes. If the current density is high, the rate of evolution of hydrogen ions at the electrode surface will be high, resulting in a high chemical potential generated in the solution.

The dependence of the anodic potential on applied current density with reverse polarity and in open circuit condition is shown in Figure 2(b). The shapes of unloading curves for all the current densities are very similar even though their time scales are different. The unloading of hydrogen from hydrogen saturated film ($\text{SmH}_{3-\delta}$) takes place in the plateau region, which is confirmed from the decreases in transmission in that region. The potential at which the plateau occurs shifts to positive values as the current density increases with reverse polarity. For the higher current density, the curve loses the sigmoid shape. No clear plateau occurs in loading of hydrogen, therefore, the unloading curves were used to study the thermodynamic properties.

An equilibrium hydrogen pressure P_{H_2} (bar) is calculated from the equilibrium potential E_e shown in Figure 2(b) using Nernst equation

$$\ln P_{\text{H}_2} = -\frac{nF}{RT}(E_e + 0.926), \quad (3)$$

where $R = 8.314 \text{ J/K mol}$ is the gas constant, $F = 96485 \text{ C/mol}$ is the Faraday constant, T the temperature, and n the number of electrons involved in the hydrogen evolution reaction ($n = 2$). This enables us to construct the pressure-composition isotherm for the samarium-hydrogen system between dihydride and trihydride, during hydrogen unloading. Figures 3 and 4 show the partial pressure of hydrogen and transmittance on unloading of hydrogen in open circuit condition and at different current densities, respectively. Pressure-composition isotherms also provide us information on enthalpies of formation. A plateau in the isotherm

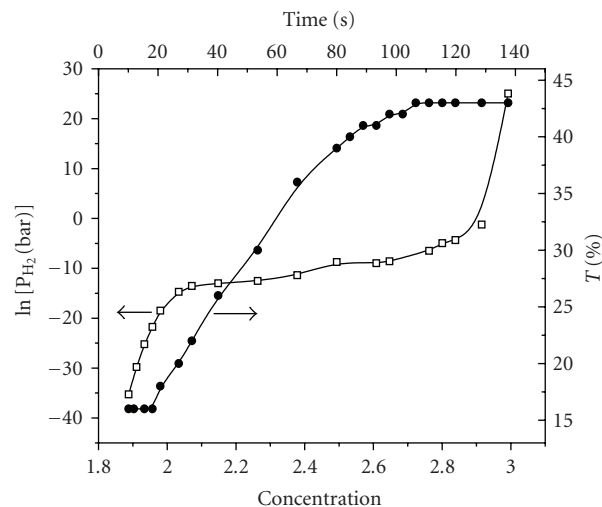


FIGURE 3: Pressure-concentration isotherm and transmission as a function of concentration during unloading in open-circuit condition.

corresponds to coexistence of two different phases, dihydride fcc and trihydride hexagonal shifts towards lower pressure with increase in applied current density during hydrogen unloading. Knowledge of these two phases, particularly those accompanying the optical change, is important for determining the mechanism of optical switching in these films. Figures 3 and 4 show the transmission of the films on unloading of hydrogen decreasing in the plateau region indicating that most of the changes in the samples take place in this region. Which can be understood by noting that in this region, the WE starts to discharge its hydrogen and that discharged hydrogen stays at the interface of WE, which is reflected in the near constant pressure of hydrogen.

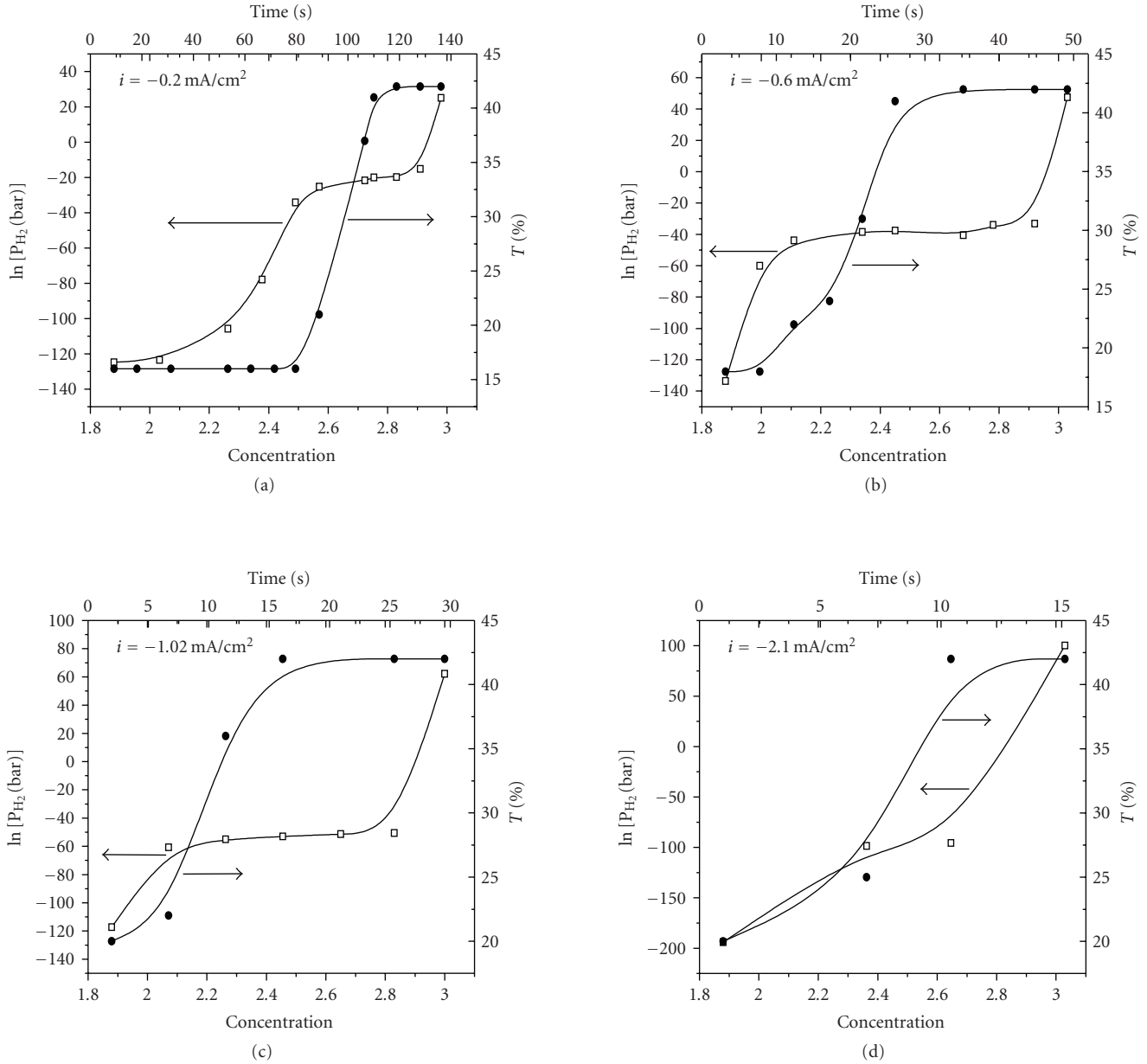


FIGURE 4: Pressure-concentration isotherms and transmissions as function of concentration at different anodization current densities.

From the plateau pressure corresponding to a coexistence region between two phases fcc and hexagonal, it is possible to estimate the corresponding enthalpy of formation of the high concentration phase with the relation

$$\Delta H = \frac{RT}{2} \left[\ln P_{H_2} - \frac{S_{H_2}^0}{R} \right], \quad (4)$$

where $S_{H_2}^0 = 130.8 \text{ J/K mol H}$ is the standard molar entropy of hydrogen gas.

From the unloading pressure-composition isotherm, the enthalpy of formation at $x = 2.6$ is -32.1 kJ/mol H in open circuit condition, while in anodically discharge of hydrogen

it is -48.4 kJ/mol H are in quite agreement with the reported value of -39.6 kJ/mol of H for the transition during samarium dihydride to trihydride state. Figure 5 shows the variation of enthalpies of formation with different current densities. The enthalpy of formation as shown in Figure 5 is linearly dependent on the current density. From these, one can attribute that the heat obtained by applying 0.2 mA/cm^2 de-loading current is -17.1 kJ/mol of H, which is also responsible for producing more stresses between the two phases results in a reorientation of the crystal grains within the film with the (002) direction perpendicular to the substrate. The induced stresses which is also responsible for fast desorption of hydrogen can be clearly seen by sharp decrease in

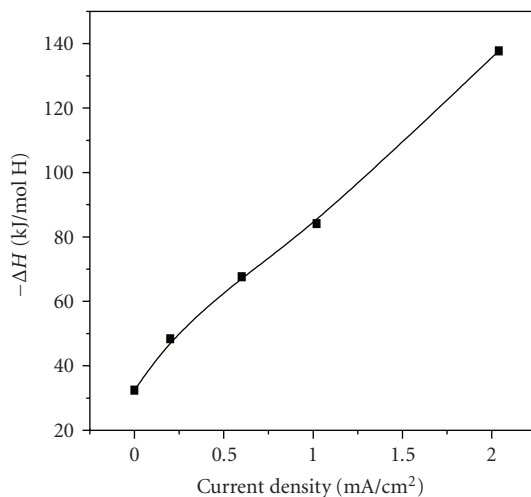


FIGURE 5: The applied current dependence of the formation enthalpy of Pd (10 nm) capped Sm (55 nm) film at $C_H = 2.6$.

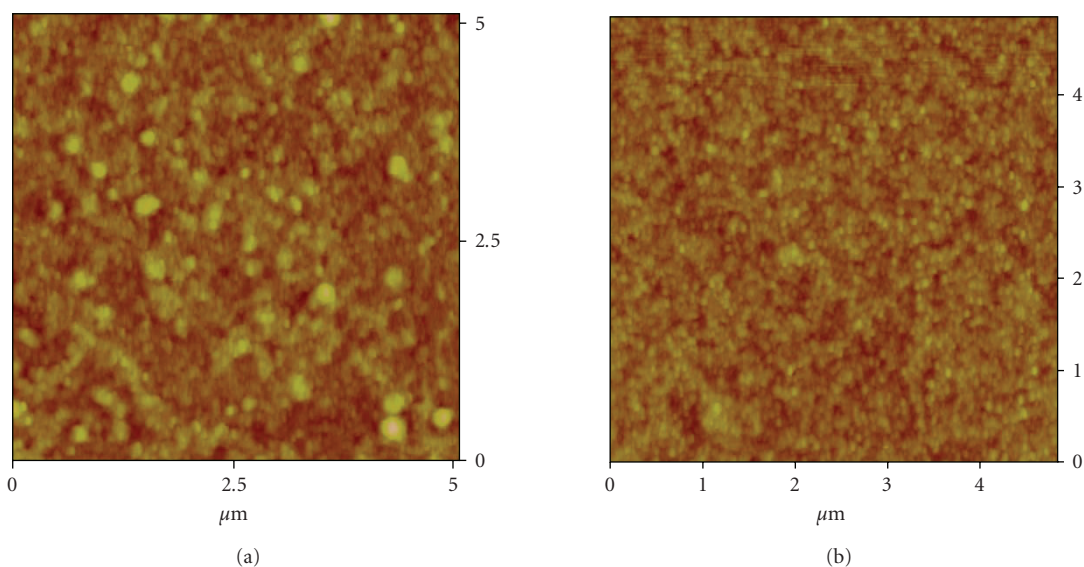


FIGURE 6: Surface morphology of Pd (10 nm) capped Sm (55 nm) hydrogen unloaded films (a) in self-discharged condition (b) in anodically discharged condition.

transmittance in anodically discharged sample compared to in open circuit discharged sample. The effect of current density was also seen in surface morphology of the hydrogen unloaded samples. Figures 6(a) and 6(b) show the surface morphology of hydrogen unloaded samples in open circuit and anodically discharged condition, respectively. There is a decrease both in rms roughness as well as crystallite size of Pd in anodically discharged sample compared to self-discharged. The rms roughness and particle size in self-discharged sample of 4.6 nm and 13 nm, respectively, decrease to 2.6 nm and 8 nm in anodically discharged sample. This decrease in both rms roughness and particle size can be due to the induced stress, developed in the film during anodically discharged of

hydrogen, and is relieved through the rearrangement of the crystal grain within the sample.

The transition time τ decreases with increasing current density. This dependence is in agreement with Sand's equation

$$\tau^{1/2} = \frac{nFA\pi^{1/2}D^{1/2}c_H}{2i}, \quad (5)$$

where D is the diffusion coefficient for the H atoms in the Sm film, A is the electrode surface area, and C_H is the hydrogen concentration. The latter was evaluated using the Faraday's law from the amount of charge supplied during different charging periods. It was found that the diffusion

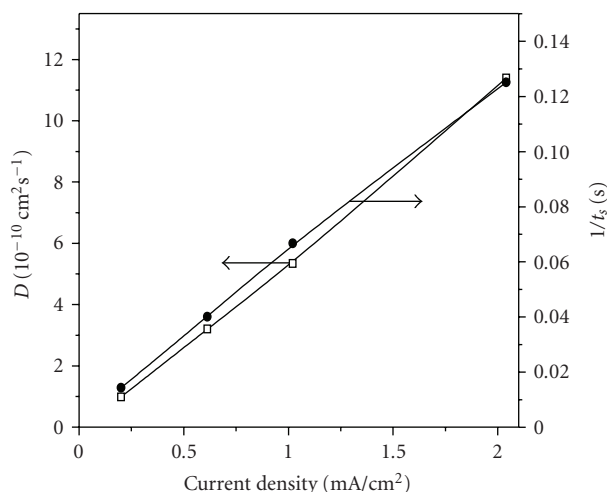


FIGURE 7: The applied current dependence of the diffusion coefficient and the reciprocal response time of Pd (10 nm) capped Sm (55 nm) film.

coefficient of hydrogen in Sm film varied with current density. Figure 7 shows the diffusion coefficient as a function of the applied current density. The diffusion coefficient increases from 9.9×10^{-10} to 11.0×10^{-10} cm²/s in the current density range from 0.2 to 2.04 mA/cm². This is of the same order as the diffusion coefficient of hydrogen in other rare earth metal films 10^{-10} to 10^{-12} cm²/s [9]. The response time decreases from 70 to 8 seconds with increasing current density. The reciprocal response time as shown in Figure 7 is also clearly inversely dependent on the current density.

4. CONCLUSIONS

It was shown that nanocrystalline Pd capped Sm films can be reversibly switched between the metallic reflecting dihydride state to semiconducting transparent (in the visible part of electromagnetic spectrum) nearly trihydride state by loading/deloading hydrogen by Galvanostatic means. Pressure-concentration isotherms of SmH_x clearly show formation plateaus. The formation of enthalpy, switching time, and diffusion coefficient has been shown to vary with applied current density. From the onset of the transmission in the isotherms, it was concluded that the deloading of hydrogen from trihydride state coincides with the transmittance decrease in plateau region, and it is therefore the final process to occur during optical switching.

REFERENCES

- [1] W. M. Mueller, J. P. Blackledge, and G. G. Libowitz, *Metal Hydrides*, Academic Press, New York, NY, USA, 1998.
- [2] J. N. Huiberts, R. Griessen, J. H. Rector, et al., "Yttrium and lanthanum hydride films with switchable optical properties," *Nature*, vol. 380, no. 6571, pp. 231–234, 1996.
- [3] R. Eder, H. F. Pen, and G. A. Sawatzky, "Kondo-lattice-like effects of hydrogen in transition metals," *Physical Review B*, vol. 56, no. 16, pp. 10115–10120, 1997.
- [4] P. J. Kelly, J. P. Dekker, and R. Stumpf, "Theoretical prediction of the structure of insulating YH₃," *Physical Review Letters*, vol. 78, no. 7, pp. 1315–1322, 1997.
- [5] K. K. Ng, F. C. Zhang, V. I. Anisimov, and T. M. Rice, "Theory for metal hydrides with switchable optical properties," *Physical Review B*, vol. 59, no. 8, pp. 5398–5413, 1999.
- [6] J. W. J. Kerssemakers, S. J. van der Molen, N. J. Koeman, R. Günther, and R. Griessen, "Pixel switching of epitaxial Pd/YH_x/CaF₂ switchable mirrors," *Nature*, vol. 406, no. 6795, pp. 489–491, 2000.
- [7] M. Kremers, N. J. Koeman, R. Griessen, et al., "Optical transmission spectroscopy of switchable yttrium hydride films," *Physical Review B*, vol. 57, no. 8, pp. 4943–4949, 1998.
- [8] E. S. Kooij, A. T. M. van Gogh, and R. Griessen, "In situ resistivity measurements and optical transmission and reflection spectroscopy of electrochemically loaded switchable YH_x films," *Journal of the Electrochemical Society*, vol. 146, no. 8, pp. 2990–2994, 1999.
- [9] M. Di Vece, I. Swart, and J. J. Kelly, "Electrochemical kinetics of hydrogen intercalation in gadolinium switchable mirrors," *Journal of Applied Physics*, vol. 94, no. 7, pp. 4659–4664, 2003.
- [10] I. A. M. E. Giebels, J. Isidorsson, and R. Griessen, "Highly absorbing black Mg and rare-earth-Mg switchable mirrors," *Physical Review B*, vol. 69, no. 20, Article ID 205111, 11 pages, 2004.
- [11] M. Ouwerkerk, "Electrochemically induced optical switching of Sm_{0.3}Mg_{0.7}H_x thin layers," *Solid State Ionics*, vol. 113–115, pp. 431–437, 1998.
- [12] T. J. Richardson, J. L. Slack, R. D. Armitage, R. Kostecki, B. Farangis, and M. D. Rubin, "Switchable mirrors based on nickel-magnesium films," *Applied Physics Letters*, vol. 78, no. 20, pp. 3047–3049, 2001.
- [13] K. Yoshimura, Y. Yamada, and M. Okada, "Optical switching of Mg-rich Mg-Ni alloy thin films," *Applied Physics Letters*, vol. 81, no. 25, pp. 4709–4711, 2002.
- [14] J. L. M. van Mechelen, B. Noheda, W. Lohstroh, et al., "Mg-Ni-H films as selective coatings: tunable reflectance by layered hydrogenation," *Applied Physics Letters*, vol. 84, no. 18, pp. 3651–3653, 2004.
- [15] F. J. A. Den Broeder, S. J. van der Molen, M. Kremers, et al., "Visualization of hydrogen migration in solids using switchable mirrors," *Nature*, vol. 394, no. 6694, pp. 656–658, 1998.
- [16] K. von Rottkay, M. Rubin, and P. A. Duine, "Refractive index changes of Pd-coated magnesium lanthanide switchable mirrors upon hydrogen insertion," *Journal of Applied Physics*, vol. 85, no. 1, pp. 408–413, 1999.
- [17] J. W. J. Kerssemakers, S. J. van der Molen, R. Günther, B. Dam, and R. Griessen, "Local switching in epitaxial YH_x switchable mirrors," *Physical Review B*, vol. 65, no. 7, Article ID 075417, 8 pages, 2002.
- [18] A. Remhof, J. W. J. Kerssemakers, S. J. van der Molen, and R. Griessen, "Hysteresis in YH_x films observed with *in situ* measurements," *Physical Review B*, vol. 65, no. 5, Article ID 054110, 8 pages, 2002.
- [19] I. Aruna, B. R. Mehta, and L. K. Malhotra, "Faster H recovery in Pd nanoparticle layer based Gd switchable mirrors: size-induced geometric and electronic effects," *Applied Physics Letters*, vol. 87, no. 10, Article ID 103101, 3 pages, 2005.
- [20] S. Enache, T. Leeuwering, A. F. T. Hoekstra, et al., "Electrical and optical properties of epitaxial YH_x switchable mirrors," *Journal of Alloys and Compounds*, vol. 397, no. 1–2, pp. 9–16, 2005.

- [21] P. H. L. Notten, M. Kremers, and R. Griessen, "Optical switching of Y-hydride thin film electrodes. A remarkable electrochromic phenomenon," *Journal of the Electrochemical Society*, vol. 143, no. 10, pp. 3348–3353, 1996.
- [22] K. von Rottkay, M. Rubin, F. Michalak, et al., "Effect of hydrogen insertion on the optical properties of Pd-coated magnesium lanthanides," *Electrochimica Acta*, vol. 44, no. 18, pp. 3093–3100, 1999.
- [23] E. S. Kooij, A. T. M. van Gogh, D. G. Nagengast, N. J. Koeleman, and R. Griessen, "Hysteresis and the single-phase metal-insulator transition in switchable YH_x films," *Physical Review B*, vol. 62, no. 15, pp. 10088–10100, 2000.
- [24] P. van der Sluis, "Chromochromic optical switches based on metal hydrides," *Electrochimica Acta*, vol. 44, no. 18, pp. 3063–3066, 1999.
- [25] C. Christofides and A. Mandelis, "Solid-state sensors for trace hydrogen gas detection," *Journal of Applied Physics*, vol. 68, no. 6, pp. R1–R30, 1990.
- [26] P. Kumar, R. Philip, G. K. Mor, and L. K. Malhotra, "Influence of palladium overlayer on switching behaviour of samarium hydride thin films," *Japanese Journal of Applied Physics*, vol. 41, no. 10, pp. 6023–6027, 2002.
- [27] P. Kumar and L. K. Malhotra, "Electrochemical loading of hydrogen in palladium capped samarium thin film: structural, electrical, and optical properties," *Electrochimica Acta*, vol. 49, no. 20, pp. 3355–3360, 2004.
- [28] J. N. Huiberts, J. H. Rector, R. J. Wijngaarden, et al., "Synthesis of yttriumtrihydride films for ex-situ measurements," *Journal of Alloys and Compounds*, vol. 239, no. 2, pp. 158–171, 1996.

Research Article

Size-Selected SnO_{1.8} : Ag Mixed Nanoparticle Films for Ethanol, CO, and CH₄ Detection

Rakesh Kumar Joshi^{1,2} and Frank Einar Kruis¹

¹*Institute of Nanostructures and Technology, Faculty of Engineering Sciences, Campus Duisburg, University Duisburg-Essen, Bismarck str.81, 47057 Duisburg, Germany*

²*Toyota Technological Institute Nagoya, Japan*

Received 21 December 2006; Accepted 28 February 2007

Recommended by Masamichi Yoshimura

Mixed nanoparticle films of SnO_{1.8} : Ag prepared by the gas phase condensation method using an aerosol route have been used for the detection of CO and CH₄. Particle size as estimated by transmission electron microscopy is 20 nm for both SnO_{1.8} and Ag nanoparticles. The gas-sensing behavior of the films for these gases has been studied in detail as a function of Ag concentration in the films. A study has been made in order to distinguish the size effect and specific surface area effect in the ethanol gas-sensing behavior of SnO_{1.8} : Ag mixed nanoparticle films. This distinction, which has not been possible using the traditional methods of the sensor fabrication, gives evidence of the dominance of size effect of the metal dopant over the surface area effect in the gas sensing of the films. The sensors show also an increased sensor signal with increase of Ag concentration in the films for CO and CH₄. It is observed from the comparative study of the sensing behavior of SnO_{1.8} : Ag films for CO and CH₄ that the sensors are more sensitive towards CO as compared to CH₄. The mixed nanoparticle films were also used for the detection of CO at 100 ppm level.

Copyright © 2007 R. K. Joshi and F. E. Kruis. This is an open access article distributed under the Creative Commons Attribution License, which permits unrestricted use, distribution, and reproduction in any medium, provided the original work is properly cited.

1. INTRODUCTION

Several methods have been used to prepare metal oxides with high surface area for conductive gas sensor applications. Conductive sensors change their conductivity when reacting with the oxidizing or reducing gases. Among the variable conductivity sensors, the metal oxides are one of the most popular technological choices. Main advantages of metal oxide sensors are a high sensitivity, long-term stability, and the possibility of integration. It is known that the gas-sensing characteristics of a metal oxide semiconductor can be improved by the introduction of metal particles on the host semiconductor material [1–4]. The interest of combining the noble metal nanoparticles with semiconductor oxides basically relies on the metal ability in acting both as sink for electrons or as redox catalyst. For this purpose, many noble metals have been introduced to the SnO_x, a most used metal oxide for gas sensors, in order to enhance the gas-sensing characteristics. The effect of metal introduction on gas-sensing properties of tin oxide has been studied in detail using metals like Pt, Pd, Au, and Ag. Amongst them Pt [2, 3] and Pd

[1] are the most used metal nanoparticles whereas Ag [5–7] have also been reported to act as catalytic particles for the gas sensing by SnO_x. We have studied the ethanol-sensing characteristics for Ag-SnO_x mixed nanoparticles in our earlier report [8–11]. The present article also reports the applicability of size selected SnO_{1.8} : Ag nanoparticles to detect CO and CH₄ gases.

In the traditional preparation techniques, it is not possible to separate the metal particle size effect and surface area effect in the metal-based metal oxides. Using a well-defined aerosol route, we made an attempt to understand the effect of the variation in metal particle size on the gas sensing of monodisperse SnO_{1.8} : Ag nanoparticle films with the variation of Ag concentration. From this study it is expected to clarify the distinction between size effect and surface area effect for the gas sensors. The distinct advantages of aerosol route over alternative methods is a very high level of control over grain size and doping level by generating both SnO_x nanoparticles as well as dopant (Ag) nanoparticles separately, selecting the desired particle sizes and then mixing them homogeneously as aerosols according to the required

Ag content in SnO_x films. Furthermore, an in-flight sintering at high temperature stabilizes the SnO_x against grain growth in the film, thereby increasing its long-term stability. The Ag particles are added to the films at the concentrations of 0.1, 1.0, and 5%, based on number concentration.

In this work, we have studied in detail the effect of Ag concentration on ethanol-sensing properties of the $\text{SnO}_{1.8}$: Ag nanoparticles prepared by aerosol route. We focus on developing a methodology in order to discriminate between size and surface effects, as we are able to vary independently the particle size and concentration. This is performed for ethanol detection. Furthermore, the detection of CO and CH_4 is shown to be feasible.

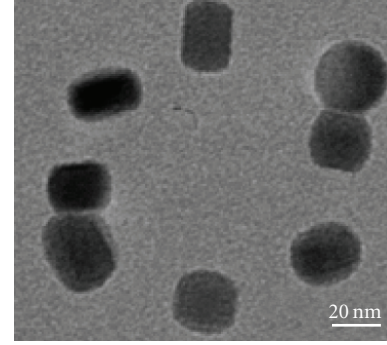
2. EXPERIMENTAL

A well-defined gas-phase synthesis method has been used for the preparation of crystalline monodisperse $\text{SnO}_{1.8}$: Ag particles [8, 9]. SnO and Ag are used as source for nanoparticles in two different furnaces. Radioactive β -source (Kr^{85}) acting as bipolar aerosol chargers were used along with differential mobility analyzers (DMA) for size classification for SnO and Ag aggregates. In the second half of the sintering/crystallization furnace (operated at 650°C) a flow of O_2 is added in order to oxidize the SnO nanoparticles to SnO_x nanoparticles, with $x > 1$. Ag is added to the films in the form of nonsintered Ag nanoparticles at the concentration level 0.1 to 5%, based on particle concentration.

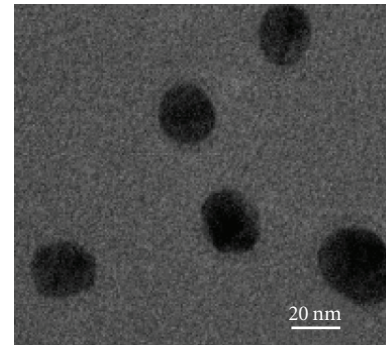
In order to deposit nanoparticle films, a precipitator was used which can act either as low-pressure impactor (LPI) or as electrostatic precipitator (ESP). The LPI has been used here for depositing $\text{SnO}_{1.8}$: Ag nanoparticle films for gas-sensing application. The method of preparation for the size-selected $\text{SnO}_{1.8}$: Ag nanoparticles for $[\text{Ag}] = 0.1, 1\%, \text{ and } 5\%$ is discussed elsewhere [8]. It is seen that the particle size for $\text{SnO}_{1.8}$ and Ag nanoparticles estimated using transmission electron microscopy was identical to the value selected by the DMA. Resistance measurements of the nanoparticle films in different gas environment were carried out by using an automated setup including a picoammeter with an internal voltage source. Details of the gas-sensing measurement setup with definitions for sensor signal, response time, and recovery times are described in previous report [8, 9, 12].

3. RESULTS AND DISCUSSION

Transmission electron microscopy (TEM) has been used for particle size determination of the $\text{SnO}_{1.8}$ and Ag nanoparticles. Figure 1 shows TEM micrographs for $\text{SnO}_{1.8}$ (Figure 1(a)) and Ag (Figure 1(b)) nanoparticles. The particle size for both $\text{SnO}_{1.8}$ and Ag nanoparticles is 20 nm. The gas-sensing properties of $\text{SnO}_{1.8}$: Ag nanoparticle films are discussed. The gases to be tested are ethanol, CO, and CH_4 , these are reducing gases. The deposition conditions were chosen such that the estimated thickness ($\sim 1.5 \mu\text{m}$) of $\text{SnO}_{1.8}$: Ag films and particle size of 20 nm for $\text{SnO}_{1.8}$ and Ag remains the same, but the Ag concentration can be varied.



(a)



(b)

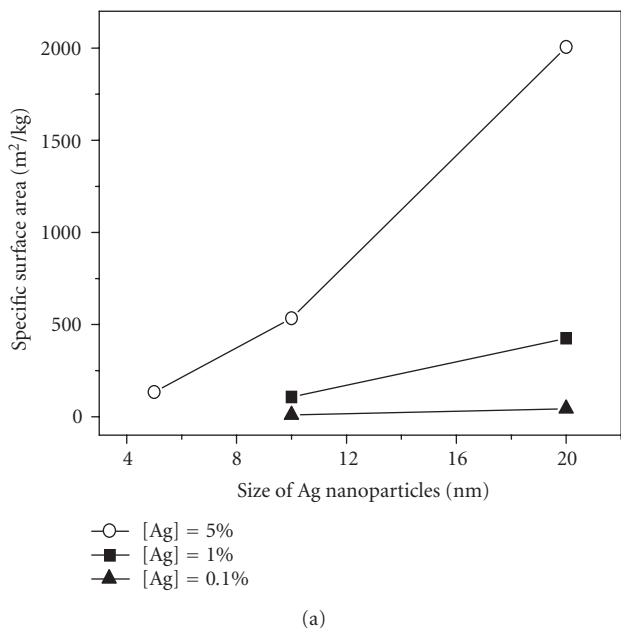
FIGURE 1: TEM micrographs for $\text{SnO}_{1.8}$ nanoparticles (a) and Ag nanoparticles (b).

The mixed $\text{SnO}_{1.8}$: Ag nanoparticle films were tested for their sensing behavior towards ethanol vapor to measure the sensor signal and response time. The sensor signal is defined as the ratio of resistance in air to resistance in ethanol gas (R_a/R_g) and response time is the time needed for the conductance of the gas sensor to obtain 90% of the maximum conductance when ethanol gas is introduced into an environment of synthetic air. We have reported an increase in the value of sensor signal and decrease in response time with an increase of Ag content in the mixed films [8, 10] for ethanol. We will now, however, concentrate on distinguishing the size effect and specific surface area effect in the ethanol gas-sensing behavior of $\text{SnO}_{1.8}$: Ag mixed nanoparticle films.

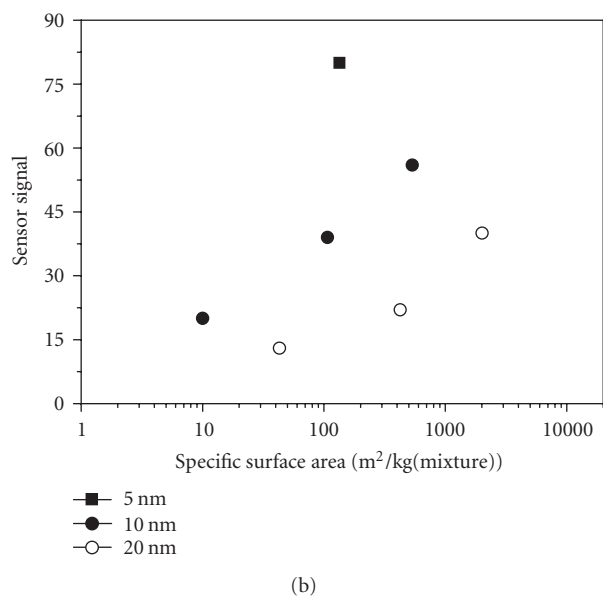
As in $\text{SnO}_{1.8}$: Ag mixed nanoparticle films, both changes in particle size as well as in the concentration will change the total surface area of the catalyst particles, we define the specific surface area (SSA) of the Ag nanoparticles, based on the total mass of the $\text{SnO}_{1.8}$ plus Ag mixture. The specific surface area values can be calculated by

$$\text{SSA (Ag in mixture)} = \frac{s_{\text{Ag}}}{(\rho_{\text{Ag}} V_{\text{Ag}} + \rho_{\text{SnO}_{1.8}} V_{\text{SnO}_{1.8}} (N_{\text{SnO}_{1.8}}/N_{\text{Ag}}))} \quad (1)$$

with s_{Ag} as the surface area of the Ag nanoparticles in m^2 and ρ , V , and N are as the density, total volume, and number of the nanoparticles of $\text{SnO}_{1.8}$ and Ag. The values of the SSA are



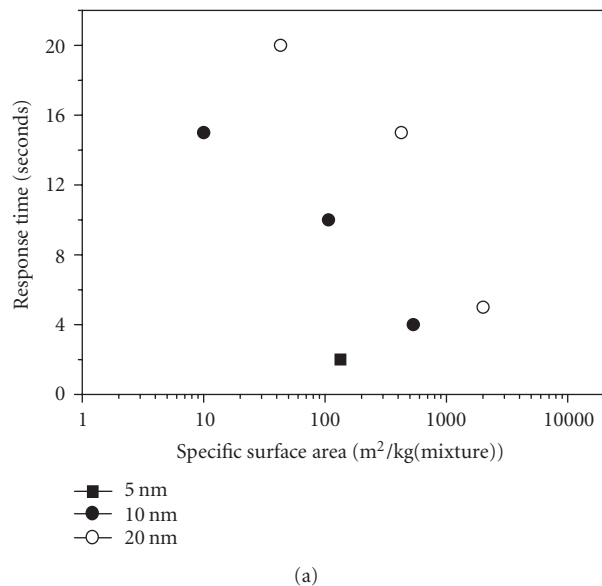
(a)



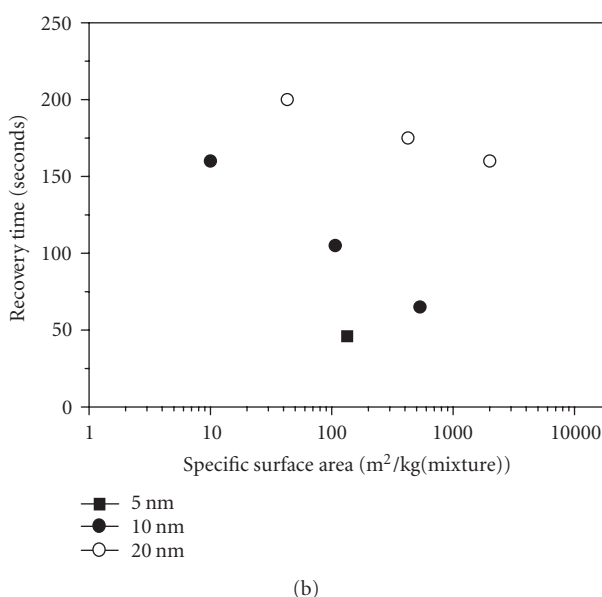
(b)

FIGURE 2: (a) Dependence of specific surface area on particle size of Ag nanoparticles for SnO_{1.8}:Ag sensors and (b) variation of sensor signal for detection of ethanol with specific surface area for SnO_{1.8}:Ag sensors (at 400°C for 1000 ppm ethanol).

plotted against the size of Ag nanoparticles in Figure 2(a). Figure 2(b) shows the variation of sensor signal with specific surface area. Here we observe an important result which is, the gas-sensor signal for ethanol increases with an increase of SSA for the mixture and decrease of Ag particle size in the mixed films. Note that on increasing the size of Ag nanoparticles the SSA increases whereas the gas-sensor signal for 1000 ppm ethanol decreases. The SSA in our mixed films is increasing due to the increase of Ag concentration in the films. Therefore, the increase of sensor signal with Ag concentration is due to the increase of available SSA whereas



(a)

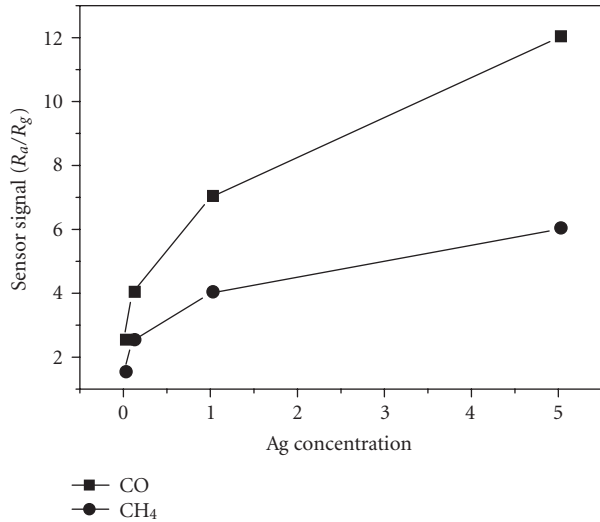


(b)

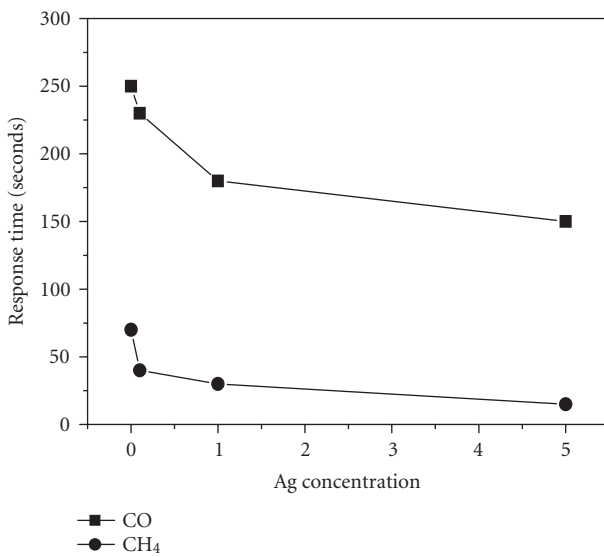
FIGURE 3: Variation of response time for 1000 ppm ethanol with specific surface area for SnO_{1.8}:Ag sensors (a) and variation of recovery time in synthetic air with specific surface area for SnO_{1.8}:Ag sensors (b).

the increase in sensor signal with reduction of particle size is a size effect rather than a surface area effect. This shows the clear evidence of the dominant nature of size effect of the metal dopant over the surface area effect on the gas-sensing behavior for the films.

The dependence of response and recovery time on the size of Ag particles and SSA of the catalyst are shown in Figures 3(a) and 3(b). The response and recovery times for the sensors with [Ag] = 5% decrease from 5 seconds to 2 seconds, and 160 seconds to 46 seconds, respectively, on decreasing the Ag particle size from 20 to 5 nm in the mixed



(a)

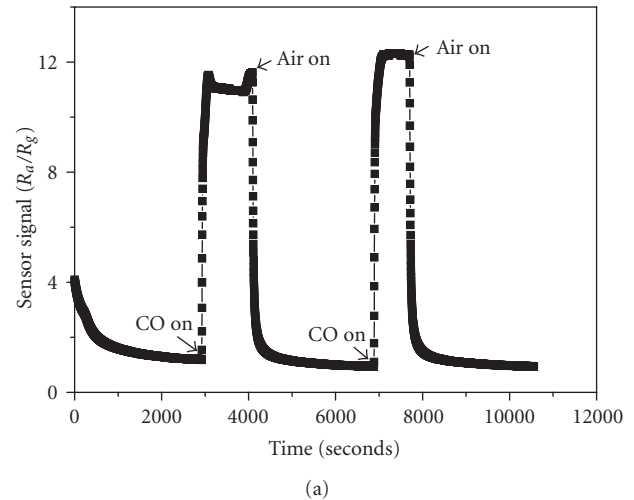


(b)

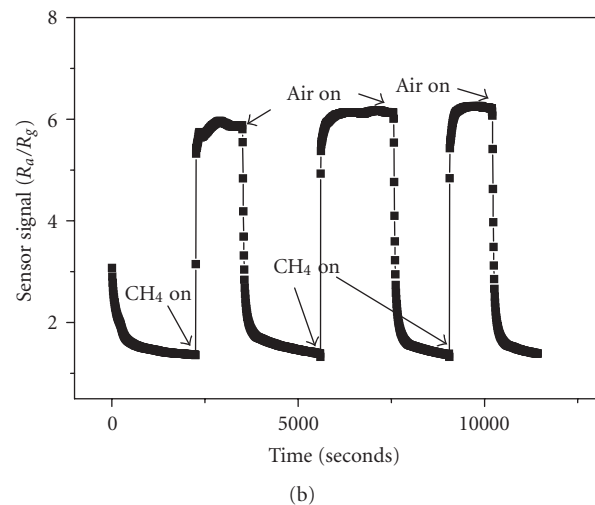
FIGURE 4: Variation of (a) sensor signal ($\text{SnO}_{1.8}$: Ag, 20 nm, 1.5 μm , $T = 400^\circ\text{C}$) and (b) response time ($\text{SnO}_{1.8}$: Ag (5%), 20 nm, 1.5 μm , $T = 400^\circ\text{C}$) for CO and CH_4 with Ag concentration for $\text{SnO}_{1.8}$: Ag nanoparticle films.

films. In the case of $[\text{Ag}] = 1\%$, response time decreases from 15 to 10 seconds and recovery time changes from 175 to 105 seconds and for $[\text{Ag}] = 0.1\%$ response and recovery times decrease from 20 to 15 seconds and 200 to 160 seconds, respectively, on decreasing the size of Ag nanoparticles from 20 nm to 10 nm in the mixed films. The stronger dependence of the response and recovery times on the Ag particle size as compared to SSA of the catalyst can be seen from the plots.

The SnO_2 -based sensors vary their conductivity in presence of oxidizing and reducing gases, because the absorption and desorption of O^- , O_2^- , and O^{2-} at the sensor surface changes the electron density at the semiconductor surface.



(a)



(b)

FIGURE 5: Sensor signal for $\text{SnO}_{1.8}$: Ag mixed nanoparticle films on repeatedly switching from synthetic air to (a) 1000 ppm CO ($\text{SnO}_{1.8}$: Ag (5%), 20 nm, 1.5 μm , $T = 400^\circ\text{C}$) and (b) 1000 ppm CH_4 ($\text{SnO}_{1.8}$: Ag (5%), 20 nm, 1.5 μm , $T = 400^\circ\text{C}$).

The adsorbed oxygen gives rise to potential barriers at grain boundaries and thus increases the resistance of the sensor surface, on the other hand reducing gases decrease the oxygen surface concentration and hence the sensor resistance. The magnitude of the response depends on the nature and concentration of the volatile molecules, and also on the type of metal oxide. An increase in the value of sensor signal and decrease in response time with increase of Ag concentration (up to 5%) for the $\text{SnO}_{1.8}$: Ag mixed films has also been observed for methane and carbon monoxide. Figures 4(a) and 4(b) show the variation of sensor signal and response time with Ag concentration in the films. It is seen that the sensors are more sensitive toward CO in comparison of CH_4 . It is interesting to note that the sensing response of the sensors is faster for CH_4 than for CO. The sensors are observed to be reproducible. Figure 5 shows the variation of sensor signal with time for $\text{SnO}_{1.8}$: Ag [5%] sensors for 1000 ppm

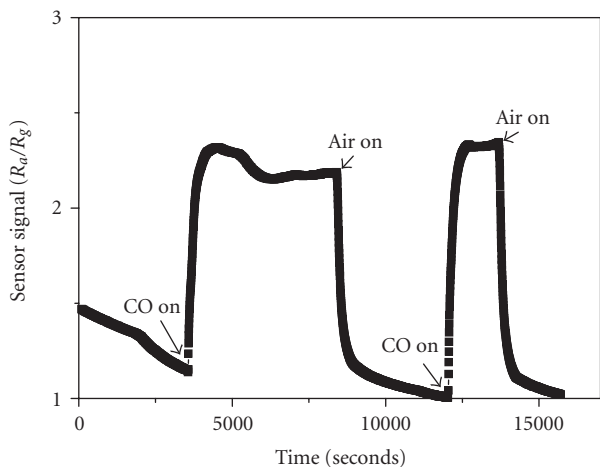


FIGURE 6: Sensor signal for $\text{SnO}_{1.8} : \text{Ag}$ mixed nanoparticle films on repeatedly switching from synthetic air to 100 ppm CO ($\text{SnO}_{1.8} : \text{Ag}$ (5%), 20 nm, $1.5 \mu\text{m}$, $T = 400^\circ\text{C}$).

CO or CH_4 . These sensors are observed to be also suitable for the CO and CH_4 based on the value of sensor signal and response time. The difference in the sensor signals for the different gaseous environment are expected to be useful for the development of gas discriminating sensors, for example, on the basis of principal component analysis or neural networks.

$\text{SnO}_{1.8} : \text{Ag}$ nanoparticle gas sensors were also tested for their potential applicability in detection of lower concentration. Response plots for $\text{SnO}_{1.8} : \text{Ag}$ [5%] in 100 ppm CO are shown in Figure 6. The response time measurements on $\text{SnO}_{1.8} : \text{Ag}$ films show a response time of 8 minutes 100 ppm CO for $[\text{Ag}] = 5\%$ sensor. It can be expected that, similar to the ethanol detection, the use of smaller Ag nanoparticles will greatly reduce this response time.

4. CONCLUSIONS

Ag particle size dependence on the gas-sensing behavior of $\text{SnO}_{1.8} : \text{Ag}$ mixed films have been studied using tailored nanoparticle films. The sensors were found to be strongly dependent on the Ag particle size. Sensors with optimized Ag concentration of 5%, and Ag particle size of 5 nm have successfully been used to detect ethanol. The gas sensor is shown to yield a different behavior in the case of exposition to CO and CH_4 . The present study is expected to be useful for developing advanced sensing materials for ppb-level gas detection, as well as gas discrimination device.

REFERENCES

- [1] N. Yamazoe, Y. Kurokawa, and T. Seiyama, "Effects of additives on semiconductor gas sensors," *Sensors and Actuators B: Chemical*, vol. 4, no. 2, pp. 283–289, 1983.
- [2] N. Yamazoe, "New approaches for improving semiconductor gas sensors," *Sensors and Actuators B: Chemical*, vol. 5, no. 1–4, pp. 7–19, 1991.
- [3] K. D. Schierbaum, J. Geiger, U. Weimar, and W. Göpel, "Specific palladium and platinum doping for SnO_2 -based thin film sensor arrays," *Sensors and Actuators B: Chemical*, vol. 13, no. 1–3, pp. 143–147, 1993.
- [4] S. Shukla, S. Seal, L. Ludwig, and C. Parish, "Nanocrystalline indium oxide-doped tin oxide thin film as low temperature hydrogen sensor," *Sensors and Actuators B: Chemical*, vol. 97, no. 2-3, pp. 256–265, 2004.
- [5] I. Kocemba and T. Paryjczak, "Metal films on a SnO_2 surface as selective gas sensors," *Thin Solid Films*, vol. 272, no. 1, pp. 15–17, 1996.
- [6] V. Lantto and J. Mizsei, " H_2S monitoring as an air pollutant with silver-doped SnO_2 thin-film sensors," *Sensors and Actuators B: Chemical*, vol. 5, no. 1–4, pp. 21–25, 1991.
- [7] C. H. Liu, L. Zhang, and Y.-J. He, "Properties and mechanism study of Ag doped SnO_2 thin films as H_2S sensors," *Thin Solid Films*, vol. 304, no. 1-2, pp. 13–15, 1997.
- [8] R. K. Joshi, F. E. Kruijs, and O. Dmitrieva, "Gas sensing behavior of $\text{SnO}_{1.8} : \text{Ag}$ films composed of size-selected nanoparticles," *Journal of Nanoparticle Research*, vol. 8, no. 6, pp. 797–808, 2006.
- [9] R. K. Joshi and F. E. Kruijs, "Influence of Ag particle size on ethanol sensing of $\text{SnO}_{1.8} : \text{Ag}$ nanoparticle films: a method to develop parts per billion level gas sensors," *Applied Physics Letters*, vol. 89, no. 15, Article ID 153116, 3 pages, 2006.
- [10] F. E. Kruijs and R. K. Joshi, "Distinction between size effect and specific surface area effect of mixed nanoparticle gas sensors," *Chemie Ingenieur Technik*, vol. 78, no. 9, pp. 1346–1347, 2006.
- [11] F. E. Kruijs and R. K. Joshi, "Nanoparticle design and handling -challenges for engineers and particle technology," *China Particology*, vol. 3, no. 1-2, pp. 99–104, 2005.
- [12] M. K. Kennedy, F. E. Kruijs, H. Fissan, B. R. Mehta, S. Stappert, and G. Dumpich, "Tailored nanoparticle films from monosized tin oxide nanocrystals: particle synthesis, film formation, and size-dependent gas-sensing properties," *Journal of Applied Physics*, vol. 93, no. 1, pp. 551–560, 2003.

Research Article

Effect of Silver Addition on the Ethanol-Sensing Properties of Indium Oxide Nanoparticle Layers: Optical Absorption Study

Vidya Nand Singh,¹ Bodh Raj Mehta,¹ Rakesh Kumar Joshi,² and Frank Einar Kruis²

¹Thin Film Laboratory, Department of Physics, Indian Institute of Technology Delhi, Hauz Khas, New Delhi 110016, India

²Institute of Nanostructures and Technology, Faculty of Engineering Sciences, Campus Duisburg, University Duisburg-Essen, Bismarckstr. 81, 47057 Duisburg, Germany

Received 21 December 2006; Accepted 11 March 2007

Recommended by Masamichi Yoshimura

In_2O_3 and $\text{In}_2\text{O}_3:\text{Ag}$ nanoparticle layers have been deposited using a two-step method consisting of chemical capping and dip coating techniques. The result of optical absorption analysis of $\text{In}_2\text{O}_3:\text{Ag}$ samples shows the presence of Ag_2O and Ag in air-annealed and vacuum-annealed samples, respectively. These results have been correlated with the gas sensing properties of these layers towards ethanol and support the proposed mechanism that increase in sensor response on Ag addition is due to the conversion of Ag_2O to Ag in the presence of ethanol.

Copyright © 2007 Vidya Nand Singh et al. This is an open access article distributed under the Creative Commons Attribution License, which permits unrestricted use, distribution, and reproduction in any medium, provided the original work is properly cited.

1. INTRODUCTION

Recently, gas-sensing properties of oxide semiconductors have been improved by preparing these materials in nanocrystalline or nanoparticle forms [1]. The sensing mechanism is based on the fact that the adsorption of oxygen on the semiconductor surface causes a significant change in the electrical resistance of the material. The formation of oxygen adsorbate (O^{-2} or O^-) results in an electron-depletion surface layer due to electron transfer from the oxide surface to oxygen. The sensing properties of oxide semiconductor materials also have been modified by adding metals or metal oxides as catalytic activator [2]. The effect of metal/metal oxide addition on gas-sensing phenomenon of oxide semiconductor has been explained in terms of doping of oxide matrix by metal atoms or formation of nano, micro, or macro-agglomerated metal clusters [3]. Various possible mechanisms have been suggested for the enhanced gas-sensing properties in presence of metal/metal oxide. In almost all studies, the structure of the metal nanoparticles in the composite nanoparticles is not well defined. In the present study, $\text{In}_2\text{O}_3:\text{Ag}$ composite nanoparticle layers have been synthesized by a two-step synthesis process using chemically grown In_2O_3 and Ag nanoparticles. Based on the detailed optical absorption studies, a possible mechanism for the effects of metal addition on the gas sensing properties

has been suggested. Formation of nanoparticles and layers in two separate steps provides the advantage of controlling the individual nanoparticle size, composition, and film thickness independently.

2. EXPERIMENTAL

Synthesis of In_2O_3 and Ag nanoparticles has been carried out by chemical capping method as discussed earlier [4–7]. The $\text{In}(\text{OH})_3$ nanoparticles were synthesized by heating 0.01 M $\text{InCl}_3 \cdot 3\text{H}_2\text{O}$ in ethanol and 0.01 M alanine in ammonia solutions (in a ratio of 1 : 2.5) at 80°C for 20 hours with continuous stirring. The nanoparticles were collected and washed several times using deionised water to remove the excess ions. This is followed by vacuum drying. In_2O_3 nanoparticles were prepared by heating $\text{In}(\text{OH})_3$ nanoparticles at 350°C. For the synthesis of Ag nanoparticles, PVP, poly (N-vinyl-2-pyrrolidone) and silver perchlorate were heated in ethanol/water mixture at 90°C with continuous stirring. Silver nanoparticles were obtained after centrifugation. $\text{In}_2\text{O}_3:\text{Ag}$ (IAG15) composite nanoparticle layers with 15 weight% Ag were prepared by a dip-coating method. The required amount of precursor nanoparticles, In_2O_3 and Ag were dispersed in ethanol. The deposited layers were dried at a temperature of 100–120°C for few minutes to evaporate out the solvents after each dip.

Glancing angle X-ray diffraction (GAXRD) analysis of nanoparticle layers was obtained using Rigaku diffractometer (Giegerflex-D/max-RB-Ru 200). A Philips CM12 electron microscope was used for transmission electron microscopy (TEM) studies. Nanoparticles were dispersed ultrasonically in water and spread over formvar coated copper grids for TEM analysis. For gas-sensing measurements, the dispersed nanoparticles were spread on substrates with interdigitated electrodes by carefully placing drops onto the substrate followed by drying in an oven at 100°C, as described elsewhere [5, 6]. Specially designed buried electrodes have been used for maintaining the homogeneity and uniformity of the nanoparticle layers. The structures are bonded to a DIL16 chip carrier through gold bond wires. A poly-Si layer, which is embedded in the structure to serve as the heating element, allows a maximum surface temperature of 300°C. An external heating arrangement has been used in order to heat the substrate to higher temperatures. A temperature-dependent resistor close to the interdigitated electrodes allows the temperature measurement. The gas-sensing properties in terms of sensor response and response time were determined by measuring the time-dependent changes in resistance on changing the gas environment in the measurement cell in the temperature range of 100–400°C.

3. RESULT AND DISCUSSION

GAXRD spectrum of composite nanoparticle layer sample IAG15 annealed at 400°C for 90 minutes is shown in Figure 1(a). The most intense peak observed in the GAXRD spectrum at $2\theta = 30.6^\circ$ belongs to (222) plane of cubic In_2O_3 . The XRD spectra of nanoparticle samples Ag and In_2O_3 annealed at 400°C for 90 minutes are shown in (b) and (c) of Figure 1, respectively. The broadening of the FWHM is due to the absence of long-range order because of the finite size of nanoparticles. TEM micrographs of samples IAG15 annealed at 400°C are shown in Figure 2. The average size of In_2O_3 and Ag nanoparticles is 13 nm and 14 nm, respectively. In the micrograph of IAG15 nanoparticle layers, the dispersion of Ag/ Ag_2O nanoparticles (relatively darker spots) in a network of indium oxide nanoparticles (less dark spots) has been marked.

Optical absorption spectra of nanoparticle layers samples In_2O_3 , Ag, and IAG15 are shown in Figure 3. The optical absorption spectrum of In_2O_3 sample shows a band edge at 305 nm characteristics of In_2O_3 nanoparticles. Spectrum of Ag sample shows a surface plasmon resonance peak at 430 nm characteristics of silver nanoparticles dispersed in PVP matrix. In the optical absorption spectrum of IAG15, both the features corresponding to In_2O_3 and the surface plasmon peak corresponding to Ag has been observed. The intensity of the absorption edge corresponding to In_2O_3 and surface plasmon resonance peak corresponding to Ag are proportional to the composition used.

The optical absorption spectrum of the IAG15 samples as-synthesized, annealed in air at 200°C, 300°C, and 400°C for 90 minutes are shown in Figure 4. The optical absorbance spectra for as-synthesized IAG15 consist of a band edge at

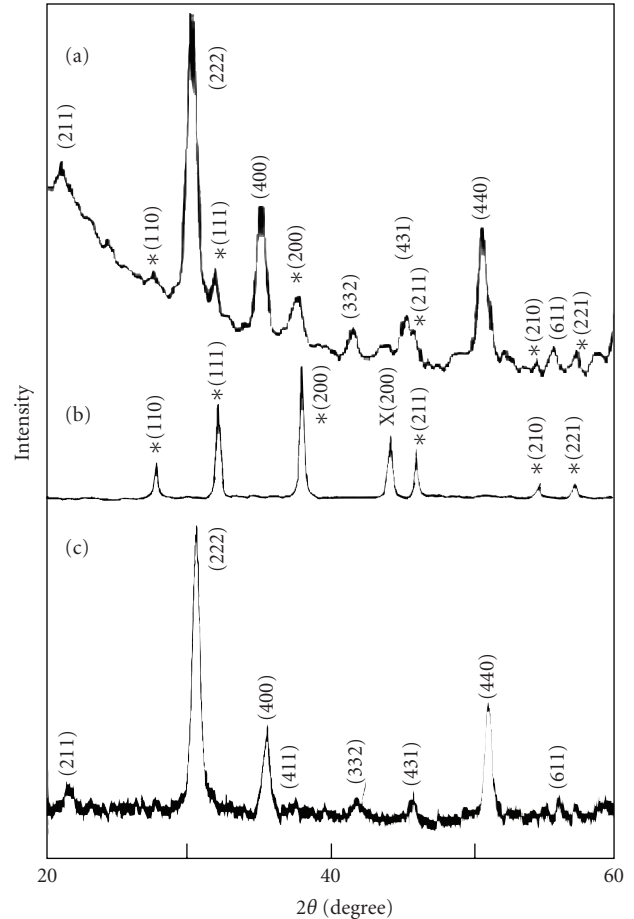


FIGURE 1: (a) GAXRD spectrum of sample IAG15, XRD spectra of (b) Ag nanoparticles sample and (c) In_2O_3 nanoparticles sample. All samples are annealed at 400°C for 90 minutes. (*) shows the peaks corresponding to the cubic Ag_2O phase and (X) shows the peaks corresponding to cubic Ag phase.

300 nm corresponding to In_2O_3 nanoparticles and a surface plasmon resonance (SPR) peak at 430 nm corresponding to silver nanoparticles. For samples annealed at 200°C, the intensity of the SPR peak decreases drastically along with the broadening of the peak. For the samples annealed at 300°C and 400°C, the peak disappears. This may be due to the conversion of Ag nanoparticles to Ag_2O nanoparticles and is consistent with the GAXRD results. It has been reported that due to a small size and increased surface to volume ratio, Ag nanoparticles have higher reactivity and they convert to Ag_2O at a temperature of 300°C in air [8]. The optical absorption spectra of the IAG15 samples annealed in vacuum at 200°C, 300°C, and 400°C for 90 minutes are shown in Figure 5. The optical absorbance spectra for samples IAG15 annealed at 200°C consists of a band edge at 300 nm corresponding to In_2O_3 nanoparticles and a surface plasmon resonance (SPR) peak at 430 nm corresponding to silver nanoparticles. For samples annealed at 300°C and 400°C, the intensity of the SPR peak decreases. In case of vacuum-annealed samples, Ag is still present and it has not

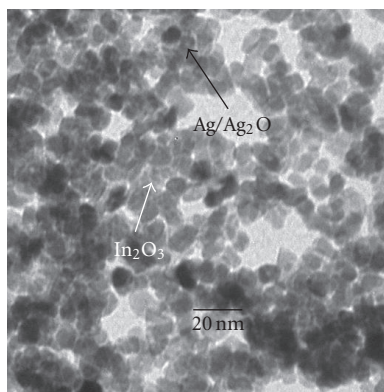


FIGURE 2: TEM micrograph of IAG15 nanoparticle layer sample annealed at 400°C for 90 minutes. The In_2O_3 as well as the Ag_2O nanoparticles are marked.

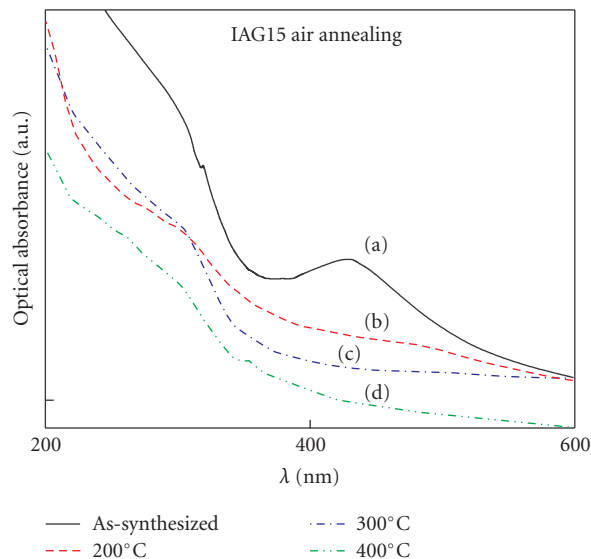


FIGURE 4: Optical absorbance spectra of the IAG15 composite nanoparticle layers (a) as-synthesized, annealed in air at (b) 200°C, (c) 300°C, and (d) 400°C for 90 minutes.

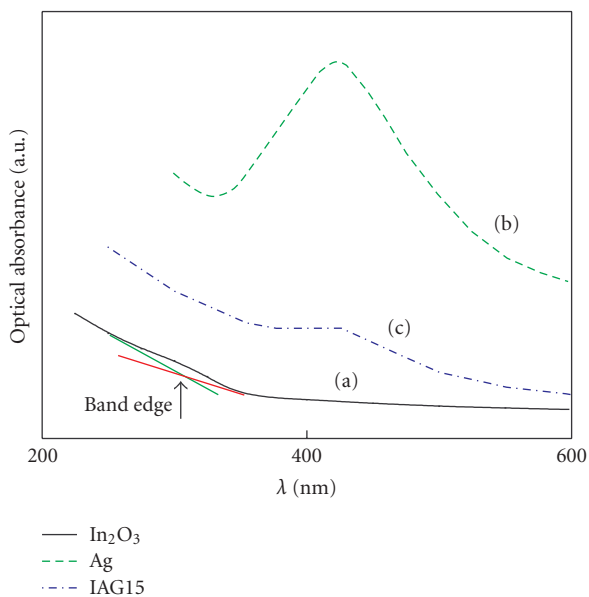


FIGURE 3: Optical absorbance spectra of the nanoparticle samples (a) In_2O_3 , (b) Ag, and (c) IAG15.

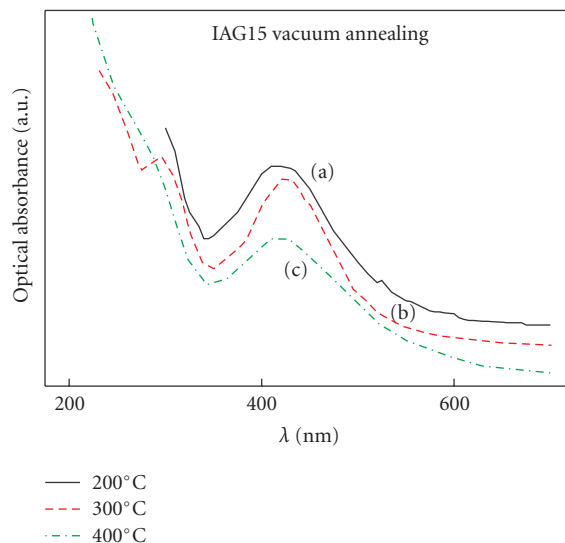


FIGURE 5: Optical absorbance spectra of the IAG15 composite nanoparticle layers annealed in vacuum at (a) 200°C, (b) 300°C, and (c) 400°C for 90 minutes.

completely converted to Ag_2O . Thus, upon annealing in air at 200°C to 400°C, the nanoparticle layers exist as $\text{In}_2\text{O}_3:\text{Ag}_2\text{O}$ and in the case of vacuum annealing they exist mainly as $\text{In}_2\text{O}_3:\text{Ag}$. The optical study has been found to be reversible and reproducible.

Figure 6 shows a comparison of the sensor response and the response time for the In_2O_3 and $\text{In}_2\text{O}_3:\text{Ag}$ nanoparticle layers at 400°C for 1000 ppm ethanol. Figure 7 shows a typical sensor response for composite nanoparticle layer. Sensor response is the ratio of the conductance of the nanoparticle layer in ethanol in synthetic air to the conductance in

synthetic air. Response time is the time required in reaching 70% of the saturated value of resistance in presence of ethanol. The sensor response in the case of IAG15 increases to 436 and the response time is about 6 seconds as compared to a sensor response of 325 and a response time of 8 seconds for In_2O_3 nanoparticle layers.

As discussed earlier, air-annealed $\text{In}_2\text{O}_3:\text{Ag}$ nanoparticle layers exist as $\text{In}_2\text{O}_3:\text{Ag}_2\text{O}$ and in vacuum-annealed samples, they exist mainly as $\text{In}_2\text{O}_3:\text{Ag}$. It is expected that the effect of exposure to ethanol vapours will be similar to annealing in vacuum. Increased gas-sensing response is thus linked with

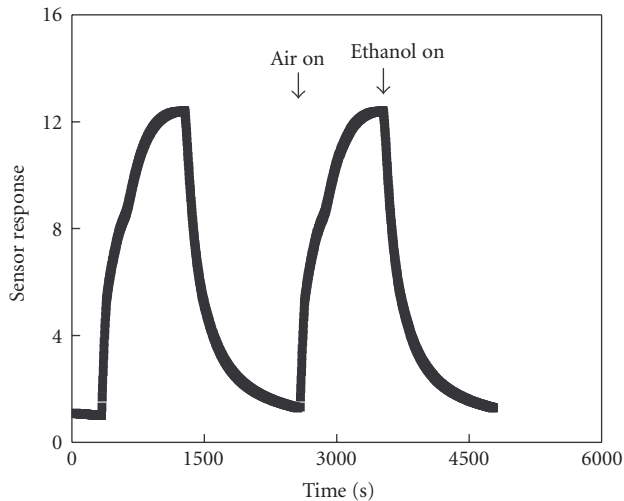


FIGURE 6: A representative gas-sensing response curve obtained with sample IAG15 for 10 ppm ethanol.

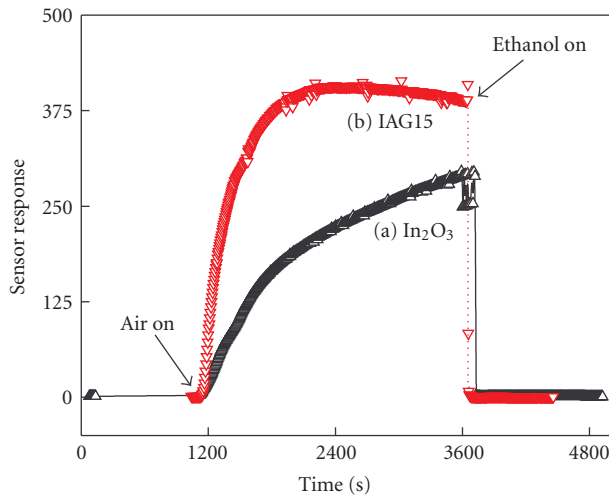


FIGURE 7: Comparison of the ethanol-sensing behavior of In_2O_3 and IAG15 nanoparticle layers for 1000 ppm ethanol at 400°C .

the transformation of depletion layer in case of $\text{Ag}_2\text{O}-\text{In}_2\text{O}_3$ interface to an accumulation layer in case of $\text{Ag}-\text{In}_2\text{O}_3$ as schematically described in Figure 8 [9]. This explains the high sensor response to ethanol in presence of Ag. In case of an In_2O_3 layer without Ag addition, gas-sensing response depends on the degree of depletion of electrons from In_2O_3 by adsorbed oxygen and the effectiveness of removal of oxygen species by ethanol. In case of In_2O_3 having appropriate amount of Ag, gas-sensing response depends upon the effectiveness of reduction of Ag_2O to Ag in the presence of reducing ambient (ethanol). The resistance in air and in 1000 ppm ethanol for the In_2O_3 and for IAG15 nanoparticle layers is 550 K Ohms, 350 K Ohms, 1.21 K Ohms, and 0.820 K Ohms, respectively. As the gas sensing mechanism is based on the interaction of sensing gas with Ag, use of Ag nanoparticles is advantageous as it provides a large

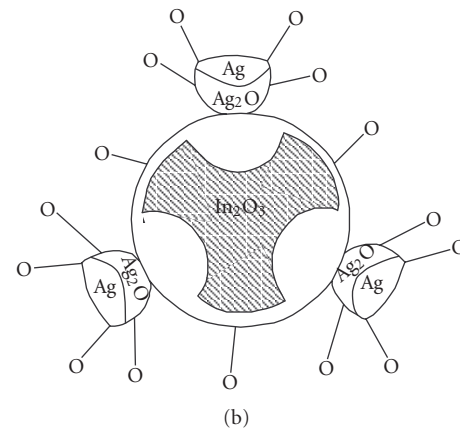
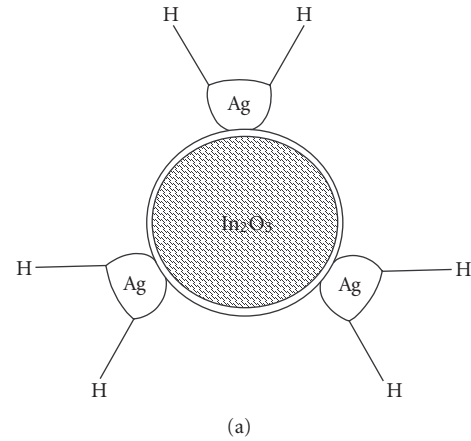


FIGURE 8: A schematic diagram showing electronic interaction at (a) $\text{In}_2\text{O}_3:\text{Ag}$ and (b) $\text{In}_2\text{O}_3:\text{Ag}_2\text{O}$ nanoparticle interfaces. In presence of ethanol, Ag_2O converts to Ag, the electron-depletion surface layer of In_2O_3 becomes smaller due to the release of the electrons to In_2O_3 , and thus the conductivity gets enhanced. In air, electron-depletion surface layer gets enhanced due to electron transfer to oxygen as well as to Ag_2O from In_2O_3 .

surface area for interaction with the sensing gas. Size of In_2O_3 nanoparticles (13 nm) used in the present study falls in the range of Debye length values estimated for oxide semiconductors [10, 11]. The nanoparticle size used is thus quite optimum for high sensor response. Use of Ag and In_2O_3 nanoparticles of approximately equal sizes is expected to result in homogenous mixing of two phases in composite nanoparticle samples. Our earlier studies have shown that particle size, structure, and the properties of the nanoparticles do not change at the operating temperature used in the present study [4, 5]. Papadopoulos et al. have reported a sensor response of 33 in In_2O_3 films for 26 ppm ethanol at 450°C [12]. Shukla et al. have reported a sensor response value of 16 for 1000 ppm H_2 at 50°C [1]. Chung et al. have reported sensor response of 88 for 2000 ppm ethanol at 350°C [13]. The high value of sensor response and faster response

observed in the present study in comparison to the reported values in various oxide semiconductors (especially, sensing response towards reducing gases) can thus be directly correlated with the electronic interaction, larger surface area due to nanoparticle nature of both the phases used in the present study.

4. CONCLUSIONS

In_2O_3 and $\text{In}_2\text{O}_3:\text{Ag}$ nanoparticle layers having well-defined particle size and composition have been prepared using a two-step synthesis method. Optical absorption studies carried out on $\text{In}_2\text{O}_3:\text{Ag}$ samples show the presence of In_2O_3 and Ag_2O phases in air-annealed samples. In vacuum-annealed samples the presence of surface plasmon resonance peak shows the conversion of Ag_2O to Ag phase. These results support the proposed mechanism based on the conversion of $\text{In}_2\text{O}_3:\text{Ag}_2\text{O}$ interface to $\text{In}_2\text{O}_3:\text{Ag}$ interface on exposure to reducing gases and explain the enhance gas sensing properties of composite nanoparticle layers.

ACKNOWLEDGEMENT

This work was supported by Council for Scientific and Industrial Research (CSIR), New Delhi, India, under Grant no. 03(0995)/04/EMR-II.

REFERENCES

- [1] S. Shukla, S. Seal, L. Ludwig, and C. Parish, "Nanocrystalline indium oxide-doped tin oxide thin film as low temperature hydrogen sensor," *Sensors and Actuators B: Chemical*, vol. 97, no. 2-3, pp. 256–265, 2004.
- [2] G. Neri, A. Bonavita, G. Rizzo, S. Galvagno, N. Donato, and L. S. Caputi, "A study of water influence on CO response on gold-doped iron oxide sensors," *Sensors and Actuators B: Chemical*, vol. 101, no. 1-2, pp. 90–96, 2004.
- [3] A. Cabot, A. Diéguez, A. Romano-Rodríguez, J. R. Morante, and N. Bárzan, "Influence of the catalytic introduction procedure on the nano- SnO_2 gas sensor performances: where and how stay the catalytic atoms?" *Sensors and Actuators B: Chemical*, vol. 79, no. 2-3, pp. 98–106, 2001.
- [4] V. N. Singh and B. R. Mehta, "Nanoparticle size-dependent lowering of temperature for phase transition from $\text{In}(\text{OH})_3$ to In_2O_3 ," *Journal of Nanoscience and Nanotechnology*, vol. 5, no. 3, pp. 431–435, 2005.
- [5] B. R. Mehta and V. N. Singh, "Structural, electrical and gas-sensing properties of $\text{In}_2\text{O}_3:\text{Ag}$ composite nanoparticle layers," *Pramana - Journal of Physics*, vol. 65, no. 5, pp. 949–958, 2005.
- [6] V. N. Singh, B. R. Mehta, R. K. Joshi, F. E. Kruis, and S. M. Shivaprasad, "Enhanced gas sensing properties of $\text{In}_2\text{O}_3:\text{Ag}$ composite nanoparticle layers; electronic interaction, size and surface induced effects," to appear in *Sensors and Actuators B: Chemical*, In Press.
- [7] V. N. Singh, B. R. Mehta, R. K. Joshi, and F. E. Kruis, "Size-dependent gas sensing properties of indium oxide nanoparticle layers," *Journal of Nanoscience and Nanotechnology*, vol. 7, no. 7, 2007.
- [8] U. K. Barik, S. Srinivasan, C. L. Nagendra, and A. Subrahmanyam, "Electrical and optical properties of reactive DC magnetron sputtered silver oxide thin films: role of oxygen," *Thin Solid Films*, vol. 429, no. 1-2, pp. 129–134, 2003.
- [9] N. Yamazoe, "New approaches for improving semiconductor gas sensors," *Sensors and Actuators B: Chemical*, vol. 5, no. 1-4, pp. 7–19, 1991.
- [10] N.-L. Wu, S.-Y. Wang, and I. A. Rusakova, "Inhibition of crystallite growth in the sol-gel synthesis of nanocrystalline metal oxides," *Science*, vol. 285, no. 5432, pp. 1375–1377, 1999.
- [11] H. Ogawa, A. Abe, M. Nishikawa, and S. Hayakawa, "Preparation of tin oxide films from ultrafine particles," *Journal of the Electrochemical Society*, vol. 128, no. 3, pp. 685–689, 1981.
- [12] C. A. Papadopoulos, D. S. Vlachos, and J. N. Avaritsiotis, "Comparative study of various metal-oxide-based gas-sensor architectures," *Sensors and Actuators B: Chemical*, vol. 32, no. 1, pp. 61–69, 1996.
- [13] W.-Y. Chung, G. Sakai, K. Shimanoe, N. Miura, D.-D. Lee, and N. Yamazoe, "Preparation of indium oxide thin film by spin-coating method and its gas-sensing properties," *Sensors and Actuators B: Chemical*, vol. 46, no. 2, pp. 139–145, 1998.

Research Article

Catalyst Composition and Content Effects on the Synthesis of Single-Walled Carbon Nanotubes by Arc Discharge

Tingkai Zhao,^{1,2} Qinghu Tang,³ Yongning Liu,¹ Changchun Zhu,² and Xiang Zhao⁴

¹ State Key Laboratory for Mechanical Behavior of Materials, Xi'an Jiaotong University, Xi'an 710049, China

² School of Electronics and Information Engineering, Xi'an Jiaotong University, Xi'an 710049, China

³ School of Energy and Power Engineering, Xi'an Jiaotong University, Xi'an 710049, China

⁴ School of Science, Xi'an Jiaotong University, Xi'an 710049, China

Received 15 January 2007; Accepted 16 March 2007

Recommended by Rakesh K. Joshi

Single-walled carbon nanotubes (SWCNTs) were prepared by a modified arc discharging furnace using Fe-Ni-Mg powders as catalyst at 600°C. The effects of catalyst composition and content on the production rate and purity of SWCNTs are investigated in this paper. When the Fe-Ni-Mg catalyst composition is 2 : 1 : 2 wt% and the catalyst content is 5 wt%, the experimental results indicate that the production of SWCNTs is 12 grams per hour, and the purity and diameter of SWCNTs are 70% and 1.22 ~ 1.38 nm, respectively. The results indicate that the cooperative function of catalyst composition and content plays an important role in the production of SWCNTs. The aim of this work is to control the production process of SWCNTs efficiently.

Copyright © 2007 Tingkai Zhao et al. This is an open access article distributed under the Creative Commons Attribution License, which permits unrestricted use, distribution, and reproduction in any medium, provided the original work is properly cited.

1. INTRODUCTION

Since the discovery of single-walled carbon nanotubes (SWCNTs) by Iijima and Bethune in 1993 [1, 2], there has promised a new field of science and technology with their specially elongated fullerene structure. But the research and application of SWCNTs have been confined in a considerable degree because of low production rate. Therefore, how to improve the production rate of SWCNTs has become a difficult work. Many researchers have carried out large amounts of significant studies on this area [2–7]. There are mainly three of synthesis methods, such as arc discharge (AD) [8], laser ablation (LA) [9], and chemical vapor deposition (CVD) [10].

For all methods, catalyst plays a very important role on the production of SWCNTs. Generally, a metal or an alloy powder as catalyst is necessary for the growth of the SWCNTs according to the growth mechanism. A suitable catalyst and other conditions can improve the production of SWCNTs. Therefore, the investigation of catalyst including its type, composition, and content is very important to control the synthesis of SWCNTs on large scale. Generally, SWCNTs are prepared by using catalysts which include transition single metal or multimetals, such as Fe, Co, and Ni or Co/Ni and Ni/Y [11–14]. All the catalysts are effective to improve the

production of SWCNTs under certain conditions. According to previous literatures [6, 7], Fe – Ni – Mg powder as catalyst is one of the more efficient catalysts to prepare SWCNTs by arc discharging furnace at controlled temperature on large scale and high purity at present. The effect of temperature on the formation of SWCNTs has been studied in detail [6]. However, the effects of catalyst composition and content on the growth of SWCNTs are not well investigated in previous paper. Therefore, it is necessary to carry out this research continuously and deeply so that we can commendably control the formation of SWCNTs. The aim of this work is to develop a control method which can synthesize SWCNTs on large scale and high purity so that they meet the needs of researches and applications.

2. EXPERIMENTAL

In our experiment, SWCNTs were prepared by arc discharging furnace at controlled temperature using a mixture of Fe-Ni-Mg powders as catalyst at 600°C [15]. The arcing current is 100A and the static helium atmosphere pressure is 500 torr. Finally, we obtained a cloth-like soot formed on the entire inner wall of the chamber and, in general, an 80 mm anode rod is used up in 10 minutes and 2 g of soot can be collected.

The catalyst powder was mixed using Fe, Ni, and Mg (all the chemical purity) elements. Then the powders were ball-milled by planetary ball miller about 30 min.

The characterization of SWCNTs were studied by using SEM(JEOL JSM-6700F), TEM(JEOL JEM-200CX), HRTEM(JEOL JEM-2010), XRD(RIGAKU D/MAX-2400, with $\text{CuK}\alpha$), and Raman scattering spectroscopy(Raman 950, with wavelength 1064 nm).

3. RESULTS AND DISCUSSION

Under the fixed conditions, such as Fe-Ni-Mg powders as catalyst, the environmental temperature of 600°C , the arc current of 100A, helium(the purity about 99.995%) as buffer gas and the pressure of 500 torr, SWCNTs were synthesized by arc discharging furnace at controlled temperature. The effects of catalyst composition and content on the formation of SWCNTs are mainly investigated.

The Fe-Ni-Mg (5 wt%) catalyst composition of (wt%): 2 : 1 : 0.5, 2 : 1 : 2, 2 : 2 : 1, 2 : 3 : 1 and 1 : 1 : 1 is studied, respectively. The results are shown in Table 1 and Figure 1.

The results from Table 1 show that the effect of catalyst composition on the production and purity of SWCNTs is obvious. With the content of Fe increasing, the production and purity of SWCNTs all decreased. That is to say, low content of Fe is effective to improve the production of SWCNTs. Meanwhile, low content of Mg is not effective to improve the production of SWCNTs, suitable Mg content can improve the production of SWCNTs. Mg has small radius and low evaporation point because the high content of Mg may increase the pressure of chamber so that the production is decreased. But the low content Mg cannot exert its action. When the catalyst composition is 2 : 1 : 2 wt%, the production of SWCNTs 12 g/h, and the relative SWCNTs purity is 80%. Therefore, the suitable catalyst composition can make the production rate and purity of SWCNTs high. The typical TEM was shown in Figure 1. Figure 1 shows that the SWCNTs have some impurities.

Then we set the condition of Fe-Ni-Mg (2 : 1 : 2 wt%) catalyst content. It is 8, 6, 5, 4, 3, 2, and 1 wt%, respectively. The results are shown in Table 2 and Figure 2.

The results from Table 2 show that the effect of catalyst content on the production and purity of SWCNTs is also obvious. With the catalyst content increasing, the production and purity of SWCNTs increase. Meanwhile, the catalyst content result (5%) is a critical point. This value is, extensive the production and purity of SWCNTs decrease. When the catalyst content is 5%, the production of SWCNTs is 12 grams per hour, and the relative SWCNTs purity is 70%. The typical TEM was shown in Figure 2.

SEM image of this carbon nanotube is shown in Figure 3. HRTEM image of them is shown in Figure 4. The XRD and Raman patterns are shown in Figures 5 and 6.

Figure 3 shows that the purified SWCNTs are very pure and the tubes congregate bundles due to the Van der Waals. HRTEM image of Figure 4 shows that the SWCNTs have high purity and the diameter is about 1.3 nm by measurement. Generally, an individual carbon tube is difficult to exist by

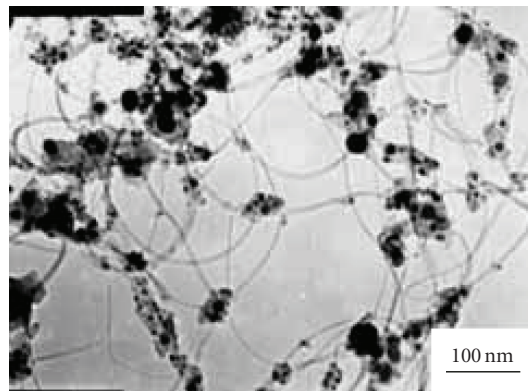


FIGURE 1: TEM image of SWCNTs produced with FeS-Ni-Mg (2 : 1 : 2) as catalyst.

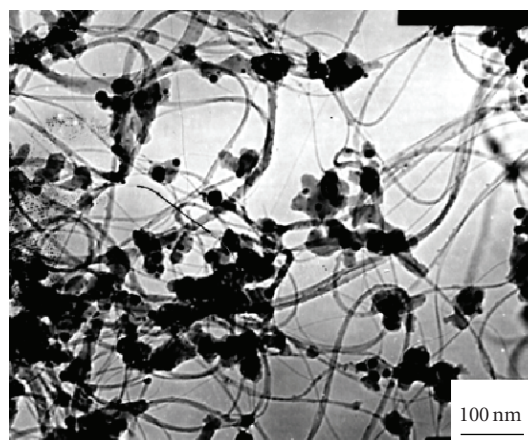


FIGURE 2: TEM image of SWCNTs produced with Fe-Ni-Mg as catalyst (5%).

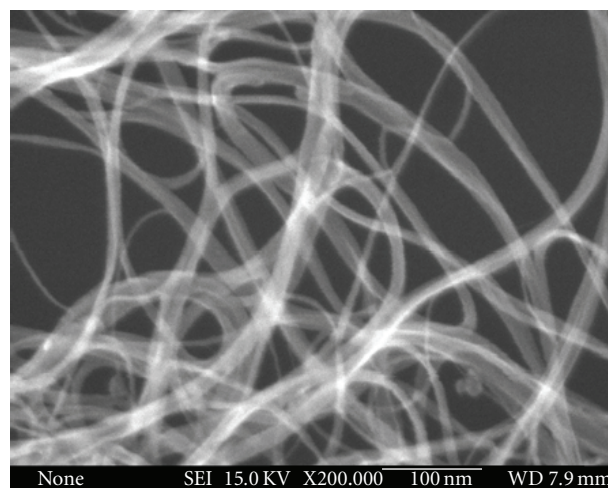


FIGURE 3: SEM image of purified SWCNTs.

TABLE 1: The effect of catalyst composition on the production and relative purity of SWCNTs.

Fe-Ni-Mg (5%) composition/wt%	production/g/h	^(a) Relative SWCNT purity (%)
2 : 1 : 2	12	80
1 : 1 : 1	10	75
2 : 1 : 1	8.3	70
2 : 2 : 1	9.7	64
2 : 1 : 0.5	7.5	60
3 : 1 : 1	8.5	48
2 : 3 : 1	5.9	1

^(a)The relative nanotube purity in sample (a) is higher than sample (b) and has increased by $x\%$.

TABLE 2: The effect of catalyst content on the production and relative purity of SWCNTs.

Fe-Ni-Mg (2 : 1 : 2 wt%) content (wt%)	production (g/h)	^(a) Relative SWCNT purity (%)
8	7.6	30
6	8.9	50
5	12.1	80
4	8.8	60
3	8.5	56
2	8	45
1	7.4	1

^(a)The relative nanotube purity in sample (a) is higher than sample (b) and has increased by $x\%$.

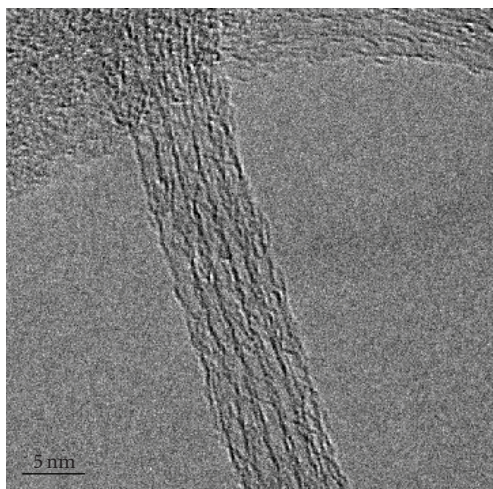


FIGURE 4: HRTEM image of SWCNTs.

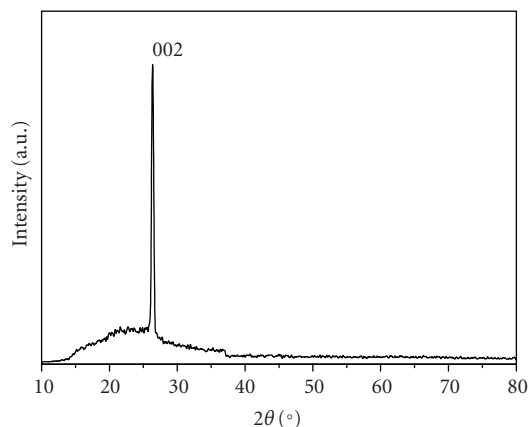


FIGURE 5: XRD pattern of SWCNTs.

the affection of electron beam while TEM or HRTEM is carried out. Therefore, a bundle of SWCNT can be seen.

XRD pattern of Figure 5 shows that the diffraction peak of the 002 face at 26.3° is sharp compared to graphite diffraction peak. The microstructure of SWCNTs has good graphite crystallinity, it is a perfectly hexagonal crystal structure. Raman patterns of Figure 6 show that the SWCNTs have two RBM peaks. The correspondence diameters are 1.38 and 1.22 nm according to $d = 224/\omega$, the RBM frequency (ω) about 162 and 183 cm^{-1} , respectively. The D-band(defect band) almost disappear, which reveals that the defective graphite structure is very low. The G-band(graphite band)

can be seen at 1592 cm^{-1} , which is a characteristic peak of carbon tube.

The results indicate that the cooperative function of catalyst composition and content play an important role in the production and the purity of SWCNTs. Compared to previous literatures, the present work only exhibits that the same catalyst which has different composition and content lead the different productions. Optimal parameters have been obtained by experimental researches. We think that moderate catalyst composition and content may enhance the dynamics process of the growth of SWCNTs. The further research of the growth mechanism will be carried out.

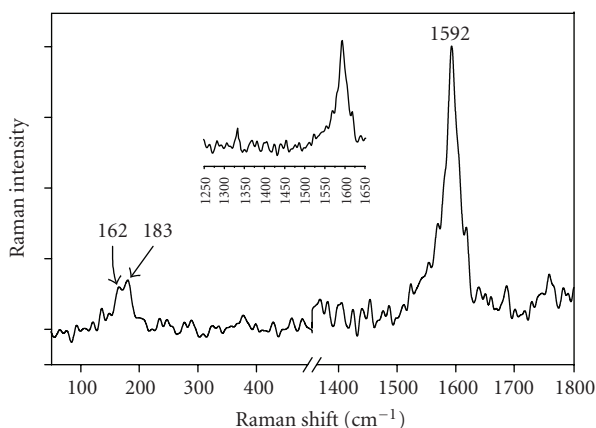


FIGURE 6: Raman pattern of SWCNTs.

4. CONCLUSION

SWCNTs were prepared by a modified arc discharge using Fe-Ni-Mg powders as catalyst at 600°C. The effects of catalyst composition and content on the production rate and purity of SWCNTs are obvious. While the catalyst composition and content are 2 : 1 : 2 wt% and 5 wt%, respectively, the production rate of SWCNTs is 12 grams per hour, and the purity of SWCNTs is about 70%. And the diameter of SWCNTs is 1.22 ~ 1.38 nm.

ACKNOWLEDGMENT

This work was financially supported by China Postdoctoral Science Foundation (Grant no. 20060391006).

REFERENCES

- [1] S. Iijima and T. Ichihashi, "Single-shell carbon nanotubes of 1-nm diameter," *Nature*, vol. 363, no. 6430, pp. 603–605, 1993.
- [2] D. S. Bethune, C. H. Kiang, M. S. De Vries, et al., "Cobalt-catalysed growth of carbon nanotubes with single-atomic-layer walls," *Nature*, vol. 363, no. 6430, pp. 605–607, 1993.
- [3] M. S. Dresselhaus, G. Dresselhaus, and P. C. Eklund, *Science of Fullerenes and Carbon Nanotubes*, Academic Press, New York, NY, USA, 1996.
- [4] T. W. Ebbesen, *Carbon Nanotubes: Preparation and Properties*, CRC Press, Boca Raton, Fla, USA, 1997.
- [5] P. M. Ajayan, "Nanotubes from carbon," *Chemical Reviews*, vol. 99, no. 7, pp. 1787–1800, 1999.
- [6] T. Zhao and Y. Liu, "Large scale and high purity synthesis of single-walled carbon nanotubes by arc discharge at controlled temperatures," *Carbon*, vol. 42, no. 12-13, pp. 2765–2768, 2004.
- [7] T. Zhao and Y. Liu, "Large scale synthesis of single-walled carbon nanotubes by an arc-discharge method at controlled temperatures," *Acta Physica Sinica*, vol. 53, no. 11, pp. 340–345, 2004.
- [8] C. Journet, W. K. Maser, P. Bernier, et al., "Large-scale production of single-walled carbon nanotubes by the electric-arc technique," *Nature*, vol. 388, no. 6644, pp. 756–758, 1997.
- [9] A. Thess, R. Lee, P. Nikolaev, et al., "Crystalline ropes of metallic carbon nanotubes," *Science*, vol. 273, no. 5274, pp. 483–487, 1996.
- [10] M. Su, B. Zheng, and J. Liu, "A scalable CVD method for the synthesis of single-walled carbon nanotubes with high catalyst productivity," *Chemical Physics Letters*, vol. 322, no. 5, pp. 321–326, 2000.
- [11] R. L. Vander Wal and L. J. Hall, "Flame synthesis of Fe catalyzed single-walled carbon nanotubes and Ni catalyzed nanofibers: growth mechanisms and consequences," *Chemical Physics Letters*, vol. 349, no. 3-4, pp. 178–184, 2001.
- [12] T. Guo, P. Nikolaev, A. Thess, D. T. Colbert, and R. E. Smalley, "Catalytic growth of single-walled nanotubes by laser vaporization," *Chemical Physics Letters*, vol. 243, no. 1-2, pp. 49–54, 1995.
- [13] B. P. Tarasov, V. E. Muradyan, Y. M. Shul'ga, et al., "Synthesis of carbon nanostructures by arc evaporation of graphite rods with Co-Ni and YNi₂ catalysts," *Carbon*, vol. 41, no. 7, pp. 1357–1364, 2003.
- [14] M. Yudasaka, N. Sensui, M. Takizawa, S. Bandow, T. Ichihashi, and S. Iijima, "Formation of single-wall carbon nanotubes catalyzed by Ni separating from Y in laser ablation or in arc discharge using a C target containing a NiY catalyst," *Chemical Physics Letters*, vol. 312, no. 2–4, pp. 155–160, 1999.
- [15] T. Zhao, "Large scale and high purity synthesis of carbon nanotubes by temperature controlled arc discharge and investigation on their growth mechanism," Doctoral dissertation, Xi'an Jiaotong University, Xi'an, China, 2005.

Research Article

Effect of Etching Parameter on Pore Size and Porosity of Electrochemically Formed Nanoporous Silicon

Pushendra Kumar and Patrick Huber

Faculty of Physics and Mechatronic Engineering, Saarland University, 66041 Saarbrücken, Germany

Received 26 December 2006; Accepted 4 April 2007

Recommended by Rakesh K. Joshi

The most common fabrication technique of porous silicon (PS) is electrochemical etching of a crystalline silicon wafer in a hydrofluoric (HF) acid-based solution. The electrochemical process allows for precise control of the properties of PS such as thickness of the porous layer, porosity, and average pore diameter. The control of these properties of PS was shown to depend on the HF concentration in the used electrolyte, the applied current density, and the thickness of PS. The change in pore diameter, porosity, and specific surface area of PS was investigated by measuring nitrogen sorption isotherms.

Copyright © 2007 P. Kumar and P. Huber. This is an open access article distributed under the Creative Commons Attribution License, which permits unrestricted use, distribution, and reproduction in any medium, provided the original work is properly cited.

1. INTRODUCTION

The increasing use of porous silicon in technological applications such as in light-emitting diodes [1], light testing equipment [2], photoelectric solar batteries [3], gas testing devices [4], microdevices [5], biological testing equipment [6], and in fundamental physics [7] has led to a particular rich area of research regarding its physical and chemical properties. The physical properties of porous silicon are fundamentally determined by the shape, diameter of pores, porosity, and the thickness of the formed porous layer. Depending on the etching parameters, for example current density, HF concentration, or substrate doping type and level, the physical properties of PS can be varied [8]. In addition, when the feature size of the pores of PS is less than a few nanometers, various quantum-size effects occur, which make PS even more fascinating. The well-studied PS morphology can range from spongy microporous (pore size < 10 nm) and branchy mesoporous silicon (pore size 10–50 nm) to the classical macroporous silicon (pore size 50 nm–20 μ m). Many theories on the formation mechanisms of PS have been reported since its discovery. Beale et al. [9] proposed that the material in the PS is depleted of carriers and the presence of a depletion layer is responsible for current localization at pore tips where the field is intensified. Smith et al. [10, 11] described the morphology of PS based on the hypothesis that the rate of pore growth is limited by the diffusion of holes to the growing pore tip. Unagami [12] postulated that the formation of PS is promoted

by the deposition of a passive silicic acid on the pore walls resulting in the preferential dissolution at the pore tips. Alternatively, Parkhutik et al. [13] suggested that a passive film composed of silicon fluoride and silicon oxide is between the PS and the silicon substrate and that the formation of PS is similar to that of porous alumina. Even though the mechanisms were different, almost all the investigators believed that the existence of holes is a prerequisite in proceeding the electrochemical polish or formation of porous silicon. The conditions for the formation of PS on all types of substrates in terms of current density and HF concentrations were reported by Zhang et al. [14], where they have shown that the formation of PS occurring during anodization was found to be dependent on the nature of electrochemical reactions. In this paper, we report the effect of the composition of etching electrolyte and applied current density on physical properties of PS. The results are presented in this paper.

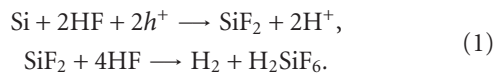
2. EXPERIMENTAL DETAILS

PS layers were prepared by electrochemical anodic etching of a highly doped *p*-type $\langle 100 \rangle$ oriented silicon substrate with a resistivity of 0.01–0.02 Ω cm. The electrochemical cell was made of Teflon and base plate was made of aluminum. A silicon wafer and a copper current collector were mounted at the bottom of the cell by using an *O*-ring that allowed 8.0 cm² of the Si surface to be exposed to the homogeneously mixed two

different concentration electrolytes composed of 4 : 6 and 6 : 4 by volume 48% hydrofluoric acid: 98% ethanol, respectively. Prior to each experiment, the Si wafers were ultrasonically cleaned in propanol and acetone. The etching current density 12.5 mA/cm^2 was applied for 7 hours. The PS thus prepared was dried by blowing Ar gas onto it. The thicknesses of the layers determined with an optical microscope were in the range of $300\text{--}310 \mu\text{m}$. The electrolyte composition of 3 : 7 by volume 48% hydrofluoric acid: 98% ethanol was also used to produce PS. But with this concentration of electrolyte, we were able to produce maximum PS thickness of $30 \mu\text{m}$. The etching of silicon in electrolyte composition of 3 : 7 was limited to a epilayer thickness of $30 \mu\text{m}$, since the porous layer peeled off whenever we tried to reach larger thickness. Therefore, this composition of electrolyte has not further been used for comparison. The prepared PS was then fixed into the homemade all-metal gas handling system that is equipped with a membrane pressure gauge of 1000 mbar full scale to study the physical properties of PS by measuring adsorption/desorption isotherms of N_2 in porous silicon at 77.2 K .

3. RESULTS AND DISCUSSION

Pores in silicon form during anodic polarization in aqueous HF solution, depending on the electrode potential and HF concentration. Many theories for pore formation mechanism have been reported in the literature [9–14]. In general, the porous silicon formation is considered to result from the inhomogeneous dissolution of the silicon surface due to competing reactions: silicon oxide formation followed by dissolution of the oxide versus a direct dissolution of silicon by HF [15]. The illustrative equation of the overall process during the PS formation can be expressed as follows:



The etching rate is determined by the holes (h^+) accumulation in the adjacent regions of the HF electrolyte and Si atoms.

The porous silicon was formed in homogeneously mixed electrolyte composed of 4 : 6 and 6 : 4 by volume hydrofluoric acid: 98% ethanol with constant applied etching current density of 12.5 mA/cm^2 for 7 hours. The mesoporous silicon prepared with different concentrations of HF was characterized by nitrogen sorption isotherms. As the change in nanorange cannot be monitored quantitatively by spectroscopic techniques, therefore the determination of the pore size distribution in mesoporous Si is usually based on the analysis of the sorption isotherms of gases at low temperature by referring to the Brunauer-Emmett-Teller (BET) model for adsorption [16, 17]. Figures 1(a) and 1(b) show the adsorption and desorption isotherms of N_2 in mesoporous silicon (prepared with different concentrations of HF) at 77.2 K (the filling fraction is plotted as function of the reduced vapour pressure p/p_0). The first part of the curve indicated by the portion AB in Figures 1(a) and 1(b) at low relative vapor pressures corresponds to the adsorption of gas on the pore

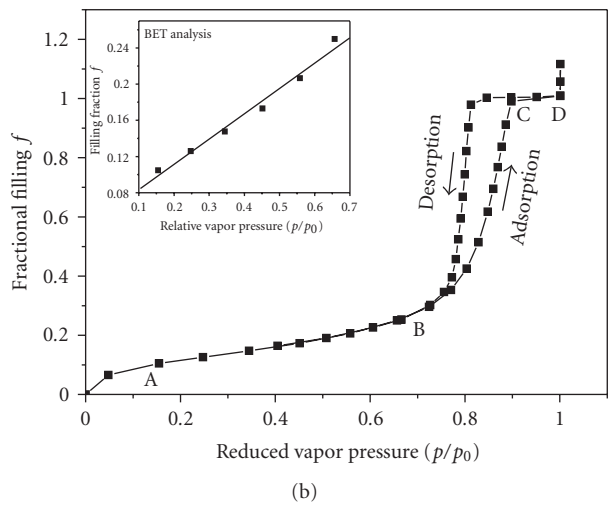
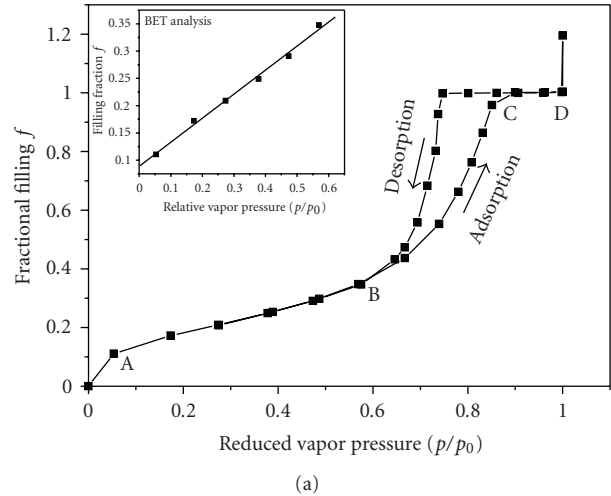


FIGURE 1: Adsorption\desorption isotherms of N_2 at 77.2 K in PS prepared at different electrolyte compositions: (a) HF : ethanol (6 : 4), (b) HF : ethanol (4 : 6). Inset in corresponding figures is the linear fit in the region AB.

wall and allows to determine the total surface area [17]. After the value of volume of nitrogen gas adsorbed on the pore wall is obtained from the isotherm, multiplication of the number of molecules required to form a unimolecular layer by the average area occupied by each molecule on the surface gives the absolute value of the surface area of the adsorbent. The region AB was linearly fitted to calculate the specific surface area by BET analysis shown in inset of the corresponding Figures 1(a) and 1(b). The sharp increase at higher relative vapor pressures indicated by the portion BC is related to capillary condensation of the gas into the pores, which is used to determine the pore size distribution. The pore size of the PS was calculated using the Kelvin equation [18]. The final plateau indicated by the portion CD shows the complete filling of the pores, and the amount of liquid corresponding to the volume of the gas adsorbed allows the determination of porosity. The hysteresis between adsorption

and desorption branches is also typical for capillary condensation. The specific surface area, pore diameter, and porosity of mesoporous silicon prepared with different concentrations of HF in electrolyte were determined using different regions of nitrogen isotherm shown in Figures 1(a) and 1(b). The pore diameter and porosity of mesoporous silicon was found to decrease with an increase of the HF concentration in the used etching electrolyte at constant applied current density. The specific surface area increases with decreasing pore diameter. The values are listed in Table 1. The physical properties of PS are determined by two large groups of factors, those that affect carrier density on the surface of a pore bottom and those that affect only the distribution of the reactions. The first group of factors includes doping type and concentration and potential. The second group of factors includes current density and HF concentration. In this report, we have varied the HF concentration and all other parameters were kept constant. On the basis of collected information from the literature [9–14], the decrease of pore diameter and porosity with increase of HF concentration in etching electrolyte can be understood as follows: for highly doped *p*-type Si, both the pore diameter and wall thickness are largely determined by the thickness of the space-charge layer formed at the interface of electrolyte and Si. Thus, in general, pore diameter has the same order of magnitude as the thickness of the space-charge layer. The wall thickness is generally less than twice the space-charge layer thickness. Because of the overlapping of the two space-charge regions entering at neighboring pores, the wall region is depleted of carriers and is thus not conductive. If the wall thickness is larger than twice the space-charge layer thickness, the walls are not depleted of carriers and dissolution can still occur to form new pores on the walls. For a PS formed for controlled space-charge layer thickness, the actual wall thickness depends on the relative dissolution rates between the edge of a pore bottom (i_b) and the pore tip (i_t). If i_b is comparable to i_t , significant dissolution occurs at the edge of the pore bottom before the pore tip propagates far away. This results in a thin wall or the annihilation of walls. On the other hand, if i_b is very small compared to i_t , the pore tip propagates relatively fast so that before much dissolution occurring on the edge of the pore bottom, the edge has already moved into the wall region where dissolution is virtually stopped due to lack of carriers. This generates relatively thick walls and small pore. For *p*-Si, increasing HF concentration reduces the thickness of the space-charge layer and increases the pore tip current density, which results in smaller pores and thicker wall. On the other hand, polishing of silicon in aqueous HF solution is known to be preceded by silicon oxide formation. The oxide is then dissolved by HF through formation of a fluoride complex in the solution. The dissolution rate of silicon oxide increases with increasing HF, which in turn increases the critical current density at which the surface is covered by oxide. As a result, the pores become smaller and walls become thicker with increasing HF concentration [15, 19]. Figure 2 shows the variation of PS layer thickness and porosity with etching time at constant current density of 12.5 mA/cm². The thickness and porosity of porous layer increase linearly with

TABLE 1: Variations of pore diameter, porosity, and specific surface area of PS with electrolyte composition at constant current density of 12.5 mA/cm².

HF	Ethanol	Pore dia. (nm)	Porosity(%)	Specific surface area
4	6	10	50	500
6	4	6	40	710

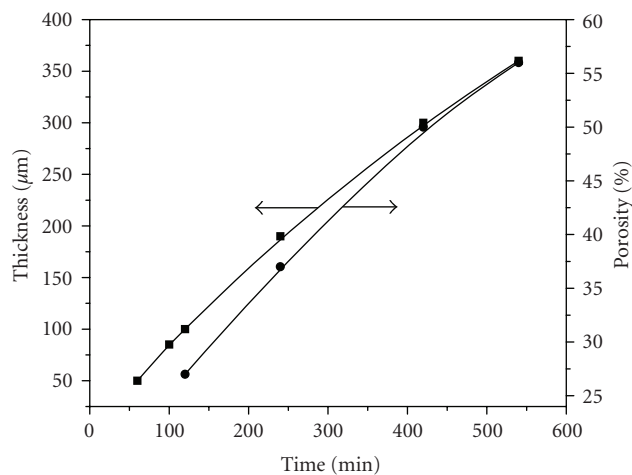


FIGURE 2: Variation of porous layer thickness and porosity with etching time at constant applied current density of 12.5 mA/cm².

etching time. It is believed that this variation in porosity with thickness is related to the chemical dissolution of the porous material during formation. During the electrochemical reaction, and as a function of the anodizing time, the effect of the chemical dissolution is to increase the average porosity and pore radii. PS was etched for one hour at different current densities and it was found that the thickness of PS layer is linearly varying with the applied current density shown in Figure 3.

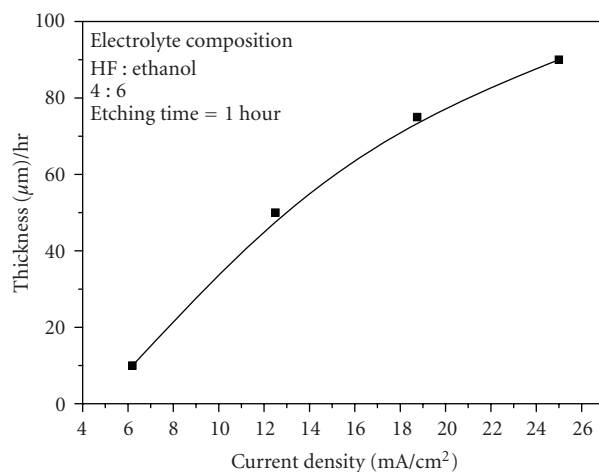


FIGURE 3: Variation of porous layer thickness with different constants applied current density for 1 hour.

4. CONCLUSIONS

Electrochemically etched mesoporous silicon formed in homogeneously mixed electrolyte of HF and ethanol was characterized by nitrogen sorption isotherms at 77.2 K, revealing that the concentration of HF in etching electrolyte plays a crucial role in controlling the physical properties of PS. It was found that the pore diameter of 10 nm and porosity of 50% of PS prepared in 4HF : 6 ethanol decreased to pore diameter of 6 nm and porosity of 40% of PS prepared in 6HF : 4 ethanol. The etching time has been found to vary both the porosity and the thickness of PS.

ACKNOWLEDGMENTS

Part of this work has been supported within the DFG priority Program 1164, Nano- and Microfluidics, Grant no. Hu 850/2.

REFERENCES

- [1] A. Richter, P. Steiner, F. Kozlowski, and W. Lang, "Current-induced light emission from a porous silicon device," *IEEE Electron Device Letters*, vol. 12, no. 12, pp. 691–692, 1991.
- [2] G. Smestad, M. Kunst, and C. Vial, "Photovoltaic response in electrochemically prepared photoluminescent porous silicon," *Solar Energy Materials and Solar Cells*, vol. 26, no. 4, pp. 277–283, 1992.
- [3] G. Willeke, H. Nussbaumer, H. Bender, and E. Bucher, "A simple and effective light trapping technique for polycrystalline silicon solar cells," *Solar Energy Materials and Solar Cells*, vol. 26, no. 4, pp. 345–356, 1992.
- [4] J. P. Proot, C. Delerue, and G. Allan, "Electronic structure and optical properties of silicon crystallites: application to porous silicon," *Applied Physics Letters*, vol. 16, no. 16, pp. 1948–1950, 1992.
- [5] V. Lehmann, "Developments in porous silicon research," *Materials Letters*, vol. 28, no. 4–6, pp. 245–249, 1996.
- [6] A. Janshoff, K.-P. S. Dancil, C. Steinem, et al., "Macroporous p-type silicon fabry-perot layers. Fabrication, characterization, and applications in biosensing," *Journal of the American Chemical Society*, vol. 120, no. 46, pp. 12108–12116, 1998.
- [7] D. Wallacher, N. Künzner, D. Kovalev, N. Knorr, and K. Knorr, "Capillary condensation in linear mesopores of different shape," *Physical Review Letters*, vol. 92, no. 19, Article ID 195704, 4 pages, 2004.
- [8] R. Herino, G. Bomchil, K. Barla, C. Bertrand, and J. L. Ginoux, "Porosity and pore size distributions of porous silicon layers," *Journal of the Electrochemical Society*, vol. 134, no. 8, pp. 1994–2000, 1987.
- [9] M. I. J. Beale, J. D. Benjamin, M. J. Uren, N. G. Chew, and A. G. Cullis, "An experimental and theoretical study of the formation and microstructure of porous silicon," *Journal of Crystal Growth*, vol. 73, no. 3, pp. 622–636, 1985.
- [10] R. L. Smith and S. D. Collins, "Porous silicon formation mechanisms," *Journal of Applied Physics*, vol. 71, no. 8, pp. R1–R22, 1992.
- [11] R. L. Smith, S. F. Chuang, and S. D. Collins, "A theoretical model of the formation morphologies of porous silicon," *Journal of Electronic Materials*, vol. 17, no. 6, pp. 533–541, 1988.
- [12] T. Unagami, "Formation mechanism of porous silicon layer by anodization in HF solution," *Journal of the Electrochemical Society*, vol. 127, no. 2, pp. 476–483, 1980.
- [13] V. P. Parkhutik, L. K. Glinenko, and V. A. Labunov, "Kinetics and mechanism of porous layer growth during n-type silicon anodization in HF solution," *Surface Technology*, vol. 20, no. 3, pp. 265–277, 1983.
- [14] X. G. Zhang, S. D. Collins, and R. L. Smith, "Porous silicon formation and electropolishing of silicon by anodic polarization in HF solution," *Journal of the Electrochemical Society*, vol. 136, no. 5, pp. 1561–1565, 1989.
- [15] X. G. Zhang, "Morphology and formation mechanisms of porous silicon," *Journal of the Electrochemical Society*, vol. 151, no. 1, pp. C69–C80, 2004.
- [16] G. Bomchil, R. Herino, K. Barla, and J. C. Pfister, "Pore size distribution in porous silicon studied by adsorption isotherms," *Journal of the Electrochemical Society*, vol. 130, no. 7, pp. 1611–1614, 1983.
- [17] S. Brunauer, P. H. Emmett, and E. Teller, "Adsorption of gases in multimolecular layers," *Journal of the American Chemical Society*, vol. 60, no. 2, pp. 309–319, 1938.
- [18] Y. C. Yortsos, in *Methods in the Physics of Porous Media*, P. Wong, Ed., chapter 3, p. 69, Academic Press, San Diego, Calif, USA, 1999.
- [19] H. Föll, J. Carstensen, and S. Frey, "Porous and nanoporous semiconductors and emerging applications," *Journal of Nanomaterials*, vol. 2006, Article ID 91635, 10 pages, 2006.